SPIN HALL EFFECT IN PARAMAGNETIC THIN FILMS

A Dissertation

by

HUACHUN XU

Submitted to the Office of Graduate Studies of
Texas A&M University
in partial fulfillment of the requirements for the degree of
DOCTOR OF PHILOSOPHY

December 2008

Major Subject: Physics

SPIN HALL EFFECT IN PARAMAGNETIC THIN FILMS

A Dissertation

by

HUACHUN XU

Submitted to the Office of Graduate Studies of
Texas A&M University
in partial fulfillment of the requirements for the degree of

DOCTOR OF PHILOSOPHY

Approved by:

Chair of Committee,	Winfried Teizer
Committee Members,	Glenn Agnolet
	Jairo Sinova
	Philip Hemmer
Head of Department,	Edward S. Fry

December 2008

Major Subject: Physics

ABSTRACT

Spin Hall Effect in Paramagnetic Thin Films.

(December 2008)

Huachun Xu, B.S., University of Science & Technology of China

Chair of Advisory Committee: Dr. Winfried Teizer

Spintronics, an abbreviation of spin based electronics and also known as magneto electronics, has attracted a lot of interest in recent years. It aims to explore the role of electrons' spins in building next generation electric devices. Using electrons' spins rather than electrons' charges may allow faster, lower energy cost devices. Spin Hall Effect is an important subfield of spintronics. It studies spin current, spin transport, and spin accumulation in paramagnetic systems. It can further understanding of quantum physics, device physics, and may also provide insights for spin injection, spin detection and spin manipulation in the design of the next generation spintronics devices.

In this experimental work, two sets of experiments were prepared to detect the Spin Hall Effect in metallic systems. The first set of experiments aims to extract Spin Hall Effect from Double Hall Effect in micrometer size metal thin film patterns. Our experiments proved that the Spin Hall Effect signal was much smaller than the theoretically calculated value due to higher electrical resistivity in evaporated thin films. The second set of experiments employs a multi-step process. It combines micro fabrication and electrochemical method to fabricate a perpendicular ferromagnet rod as a spin injector. Process description and various techniques to improve the measurement sensitivity are presented. Measurement results in aluminum, gold and copper are presented in Chapters III, IV and V. Some new experiments are suggested in Chapters V and VI.

To my wife Chuanji Zhang, my son David

and

all my family members in China

ACKNOWLEDGMENTS

I would like to express my appreciation to my advisor, Dr. Winfried Teizer, for the opportunity to work under his guidance and for the opportunity to work on Spin Hall Effect experiments. Without his guidance, encouragement, and support, none of the work could have happened. Winfried is a great teacher with a lot of techniques and ideas. I am amazed by his critical thinking ability and analytical skills. I am fortunate to be his student.

I thank Dr. Glenn Agnolet, Dr. Jairo Sinova, and Dr. Philip Hemmer for their valuable time to serve on my advisory committee. Special thanks to Dr. Glenn Agnolet and Dr. Jairo Sinova for answering my questions experimentally and theoretically. I would thank Dr. Philip Hemmer, Dr. Mosong Cheng, Dr. Joseph Ross, Dr. Donald Naugle, and Dr. Dayar Rathnayaka, just to name a few, for their valuable discussions and encouragement.

I have to extend my thanks to my colleagues in Nanolab. Arlene Ford always maintained the electron beam lithography system in good conditions and helped me on electron beam lithography patterning. John Noel was involved in the phase I experiments mainly presented in Chapter III. Joel Means, Bing Bai contributed to the earlier experimental preparations. I want to thank Kyongwan Kim, Raj Srivastava, Tracey Wellington, Luohan Peng, and Dongmin Seo for their comments and suggestions regarding this work.

Dr. Wenhao Wu, and his students Dr. Zuxin Ye, Haidong Liu, and Hong Zhang let me using their electroplating systems and generously provided valuable suggestions when I built an electroplating system. The machine shop and the electronic shop in the Physics Department helped a lot on instrument design and system calibration. Thanks to all my friends in both in the US and China for their continuous encouragement during the past years.

Finally, I would like to thank my family for supporting me in many ways. Special thanks to my wife, Chuanji, and my lovely son, David, for their support and love.

TABLE OF CONTENTS

Page

CHAPTER

LIST OF FIGURES

Page

Page

LIST OF TABLES

CHAPTER I

INTRODUCTION

1.1 Spintronics

Spintronics[1-6], an abbreviation of spin based electronics and also known as magneto electronics, attracts a lot of interest in recent years. It aims to explore the role of electrons' spins in designing the next generation electric devices. Using electrons' spins rather than electrons' charges may allow faster, lower energy loss devices. Spin current is non-dissipative and spin devices are sometimes more effective.

Traditional charge based electronics has changed the world significantly. It fuels the train of civilization. However, in semiconductor industry, as the dimensions of transistors are shrunk to smaller (nanometer size) scales in order to integrate more transistors on a chip, problems arise. One big problem is device heating. This results from the higher resistance of devices due to their smaller size. On one hand, the temperature of devices can reach a regime where they malfunction. On the other hand, a lot of energy is wasted. Although a smaller current is used to reduce the heating effect, there is always a threshold current for the devices to work. The study of non-dissipative devices is thus of great importance[7]. The electron's spin is a quantum

---

This dissertation follows the style and format of Physical Review Letters.

mechanical parameter, and a spin current is non-dissipative.

On the other hand, spin based electronics may be faster and more favorable than traditional charge based electronics. The discovery of Giant magnetoresistance (GMR)[8, 9] is considered as the birth of spintronics. Magnetoresistance (MR) is the change in the electrical resistance of a material in the presence of a magnetic field. All metals have an inherent magnetoresistance[10] due to the effect of Lorentz force. Usually the magnetoresistance effect is very small. However, metallic alloys containing magnetic atoms have an enhanced MR because the scattering in the material is controlled by the magnetic field. Experiments [8, 9] on layered and granular materials have shown an even more dramatic MR effect (GMR), which quickly found its applications in computer hard drives. Traditionally, permalloy is used for magnetoresistive sensors in hard disk reading heads in computers. After GMR was discovered in 1988, engineers successfully developed hard drive reading heads based on GMR effect. The GMR ratio has a typical value greater than 10% at room temperature. Anisotropy Magnetoresistance (AMR), the effect used in older computer hard drives, usually is less than ~3%. Therefore, replacing AMR reading heads with GMR reading heads led to a rapid increase in storage density. IBM was the first producer to market computer hard drives based on GMR technology. In 2002, IBM announced that they could compress massive amounts of data into a small area at a density of about 1.5Gbit/mm^2. Magnetoresistive Random Access Memory (MRAM), the next spintronics device of major significance, is under development since the 1990s. It is expected to enter the market soon. At the same time, scientists and engineers in industry are developing other types of spintronics devices [11]. This is an active area, both in fundamental research and in industrial applications.

1. 2 Spin Hall Effect

Great progress has been made in spintronics since 1988. Yet this area is still in its infancy. Fundamental research is needed to better understand this subject. The primary requirement to design a spintronics device is to have a system that can generate a spin polarized current, and a system that is sensitive to the spin polarization. Spin Hall Effect is one of the research areas that targeted to these questions.

Spin Hall Effect (SHE) was first proposed by Dyakonov and Perel [12, 13] in 1971, and more recently revived by Hirsch[14] in 1999 and Zhang[15] in 2000. These early theoretical works studied extrinsic Spin Hall Effect originating from asymmetrical scattering by impurities. After scattering from impurities, electrons with spins up are preferentially scattered to one direction, while electrons with spins down are scattered to the other direction so that a spin current exists perpendicular to the current flowing direction. This effect is called extrinsic Spin Hall Effect to differentiate the more recently proposed intrinsic Spin Hall Effect[16, 17]. In the intrinsic Spin Hall Effect, spin current perpendicular to the electrical current direction appears as a result of band structure in a clean system. This new phenomenon has generated extensive theoretic debates in the past several years[18].

To understand the Spin Hall Effect, we borrow basic ideas from Anomalous Hall Effect (AHE). In ferromagnetic metals, the Hall resistivity is empirically fitted by $\rho_H=R_oB+4\pi R_sM$, with $B=\mu_0H$ being the magnetic induction and H being the magnetic field, M being the magnetization per unit volume and R_o and R_s being the ordinary and anomalous Hall coefficient respectively. The microscopic origin of R_s is not well understood[19, 20]. However experimentally it has been demonstrated that electrons with magnetic moments (spins) experience a transverse force when they are moving in a longitudinal electric field (Figure 1.1a). Furthermore, electrons with opposing spin directions are subjected to forces in opposing directions. Anomalous Hall Effect appears because there are unequal numbers of spin-up VS spin-down electrons in ferromagnetic materials. Hirsch[14] argued that the same mechanism that leads to Anomalous Hall Effect in a ferromagnetic material exists in a paramagnetic material, so that spin up electrons are scattered to one direction while spin down electrons are scattered to the other direction (Figure 1.1b). Therefore, in a thin current strip, a spin imbalance exists on the two edges of the current strip. Due to the equal amount of spin up and spin down carriers in paramagnetic materials, no charge imbalance exist, unlike the Anomalous Hall Effect in ferromagnetic materials. To detect this spin imbalance experimentally is a challenging task. A voltage measurement across the current strip is not suitable for this experiment. Electrons' spins are magnetic moment. The spin imbalance across the current carrying strip leads to different magnetization, very small, at the two edges. Commercially available magnetometers at the current market do not have the high resolution to detect the magnetization difference.

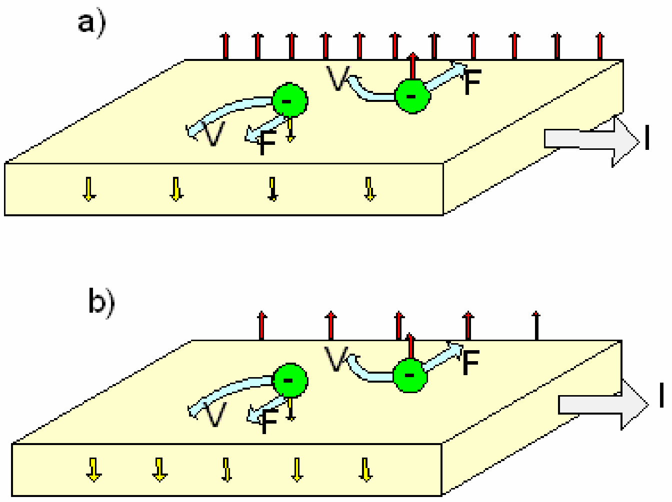

Figure 1.1 Anomalous Hall Effect and Spin Hall Effect. a) Anomalous Hall Effect in magnetic system. More carriers are deflected to one side, leading to a spin and charge imbalance. b) Spin Hall Effect in nonmagnetic system, the number of carriers with spin up equals the number of carriers with spin down. Like AHE, different spin categories are scattered differently. Charge imbalance does not exist.

1. 3 Reported experimental progresses

Although Spin Hall Effect was intensively studied theoretically, only a few experimental groups claimed to have observed the effect so far. Two groups [21, 22] observed the Spin Hall Effect in semiconductor systems using optical techniques. Lately another two groups [23, 24] reported observations of the Spin Hall Effect in metallic systems. These four experiments are briefly presented.

1.3.1 Observations in semiconductor systems

In 2004, a Santa Barbara group led by D. D. Awschalom reported the first experimental observation of Spin Hall Effect. The authors fabricated a thin n-GaAs slab with Molecular Beam Epitaxy and drove current through. The semiconductor slab has a width w=77µm, a length l=300µm, and a mesa height h=2.3µm (Figure 1.2a). The authors used Scanning Kerr Microscopy to detect the spin accumulation on the sample. The sample was illuminated with a linearly polarized laser beam. Kerr effect says that the rotation of the polarization direction of the reflected laser beam is proportional to the magnetization direction of the illuminated surface. The net magnetization is due to accumulated electrons' spins in this experiment. The focused laser beam, with a spot size of about 2µm, was scanned across the sample and the angle of Kerr rotation was measured for each position. They observed the Kerr rotation had a sign difference (Figure 1.2a) at the two edges of the slab, which suggested different types of spin accumulation at the two edges of the current carrying strip.

This Kerr rotation at the two edges of the sample was modulated by an external magnetic field which is shown in Figure 1.2b. The projection of the spin polarization to the z-axis slightly disappeared in an applied magnetic field along x direction. This was explained as spin precession in the magnetic field.

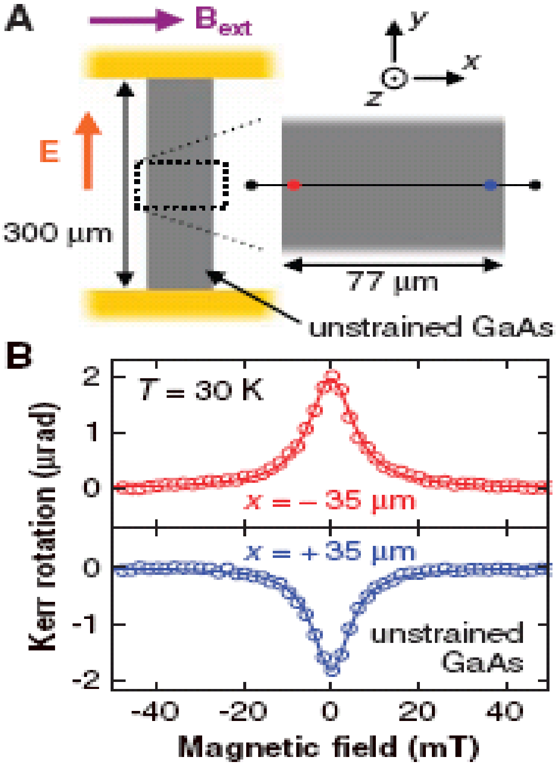

Figure 1.2 Spin Hall Effect in unstrained GaAs. Sample measured at *T*=30K. A) Schematic of the unstrained GaAs sample and the experimental geometry. B) Typical measurement of Kerr Rotation as a function of *Bext* at *x*=-35µm(red circles and *x*=+35µm(blue circles) for *E*=10mv µm^{-1}. From Ref. 21.

The focused laser beam scanned across the sample, and the Kerr rotation at each point was recorded. The spin density was mapped from the Kerr rotation at each point (Figure 1.3a). It is observed that spin density depends on position.

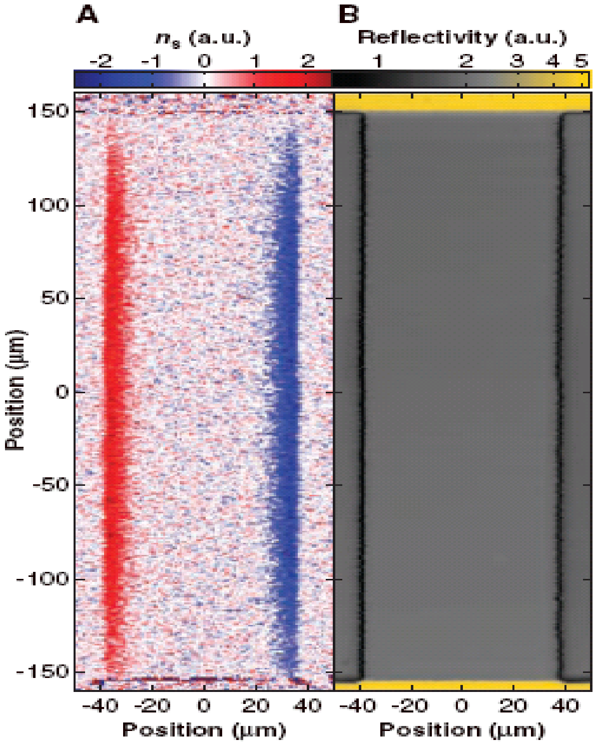

Figure 1.3 Two-dimensional image of spin density ns and reflectivity R. Sample measured in unstrained GaAs sample at *T*=30K and *E*=10mv μm^{-1}. From Ref. 21.

In the experiment, the authors did not see an influence of strain in another sample, which led them to believe the observed effect was extrinsic Spin Hall Effect. Dr. Awschalom's group observed Spin Hall Effect in similar system using the same experimental techniques[25, 26].

Almost at the same time as Dr Awschalom's work was published, an independent group[22] mixed with experimentalists and theorists reported their observation of Spin Hall Effect in a two-dimensional hole system. In this work, the authors adopted the principle of Light Emitting Diode, but changed the design to a coplanar structure with two p-n junctions. A Light-Emitting Diode [27] consists of a chip of semiconductor materials doped with impurities to create a p-n junction. When the LED is forward biased, electrons meet holes and emit light, which then passes through the material. If the electrons and holes are polarized, the emitted light is circularly polarized. The 2d-hole channel lays side above n-doped AlGaAs (Figure 1.4).

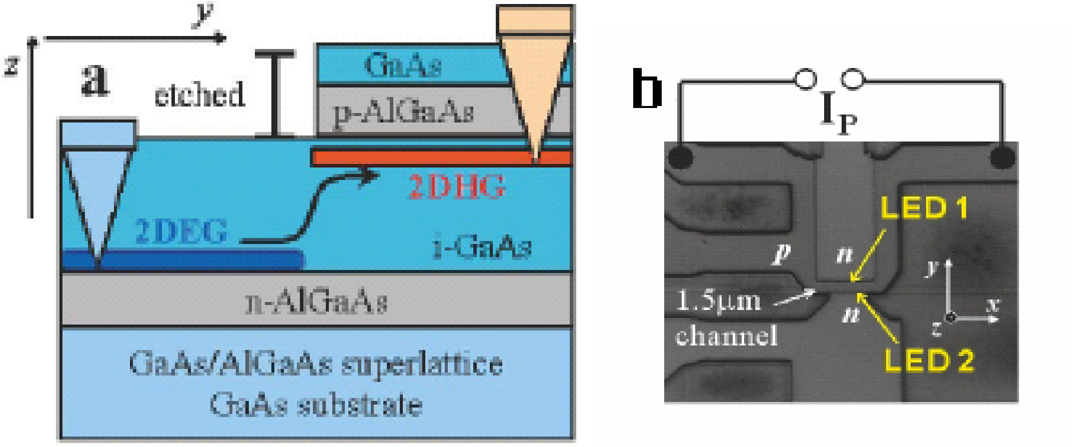

Figure 1.4 SEM images of co-planar LED devices. a) A schematic cross section view of a coplanar p-n junction LED device. b) Scanning Electron Microscopy image of the LED device. From Ref. 22.

When spin polarized holes accumulates at the edge of the channel presumably due to the Spin Hall Effect, they combine with electrons coming from the below n-AlGaAs and emit polarized light. The polarization of the light originated from the edges of the LED was measured by electroluminescence technique. The authors found that the direction of polarization was reversed as reversing the applied electric field (Figure 1.5a), and the polarization directions were opposite at the two edges (Figure 1.5b) of the hole channel which indicated the existence of Spin Hall Effect in the system. This work is in a clean system without impurities, and the observed effect is believed to be intrinsic Spin Hall Effect.

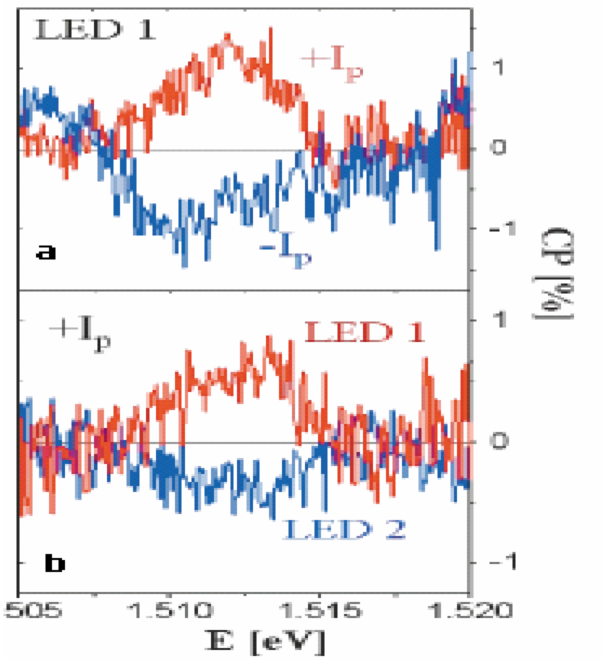

Figure 1.5 Optical measurement of Spin Hall Effect in 2d-hole system. a)Polarization direction measured with opposite current directions. b) Polarization measured at opposite edges of the hole channel. From Ref. 22.

1.3.2 Observations in metallic systems

Optical techniques are good friends to semiconductor systems, but they are not suitable for metallic systems. The main reason is that the spin diffusion length of metals is very short; usually less than 1μm in amorphous thin film. Laser beam usually has a focus spot of a few micrometers, which means that the electrons in metals lost spin coherence even within the size of the laser spot. Two experimental groups have observed the Spin Hall Effect in metallic systems using electric methods.

Valenzuela and Tinkham[23] reported their measurement of Spin Hall Effect in aluminum thin film. Their system consisted of two ferromagnetic (CoFe) electrodes and an aluminum hall cross, Fig 1.6a.

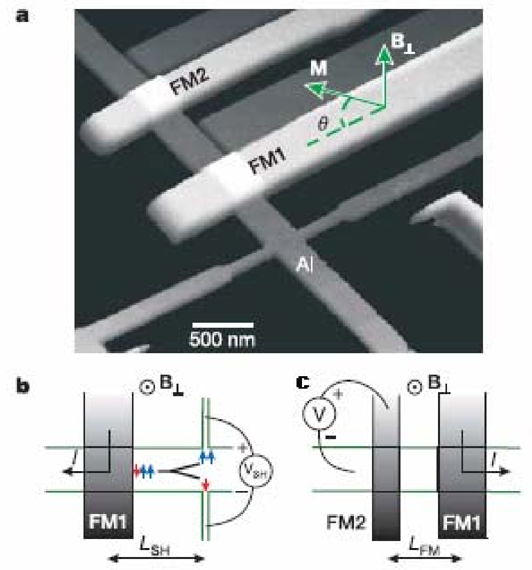

Figure 1.6 Schematic of a spin valve device. a) Atomic force microscope image of the device. Two Ferromagnetic electrodes (FM1 and FM2) on top of a thin aluminum (Al) hall cross. b) Schematic of the Spin Hall Effect measurement. c) Spin-transistor measurement for device. From Ref. 23.

The sample shown in Figure 1.6a was patterned by electron beam lithography and a two-angle shadow-mask evaporation without breaking the vacuum[28]. A MMA/PMMA pattern was first created using electron beam lithography. The aluminum cross, with arms 400nm and 60nm wide, was first deposited at normal incidence onto a Si/SiO$_2$ substrate using e-gun deposition. The aluminum film was then oxidized in pure oxygen at a pressure of 150millitor for 15mins. After the vacuum was recovered, the ferromagnetic electrodes were deposited with an angle of 50° from the normal to the substrate surface. As a result, the aluminum oxide layer between the ferromagnetic electrodes and aluminum film formed tunnel junctions. It has been demonstrated that the tunnel barrier is crucial for spin polarized tunneling because it assures a uniformly distributed injection current and enhances the spin polarization rate [28, 29].

The two ferromagnetic electrodes were used as a typical spin transistor measurement[28, 30-32] to calibrate the device. The spin-transistor measurement, was first demonstrated by Mark Johnson [31] to measure the spin diffusion length in an aluminum single crystal bar. The measurement geometry is shown in Figure 1.7a. The current is injected from FM1 into the left side of the aluminum film. The voltage between the FM2 and the right side of the aluminum film is measured. The magnetic field is applied in the sample plane. The easy axes of the ferromagnetic electrodes are in the sample plane because of the shape anisotropy of the electrodes. The geometry difference of the two ferromagnetic electrodes causes a slight difference in coercive field. Parallel and anti-parallel magnetization in the ferromagnetic electrodes could be achieved by sweeping the magnetic field in the plane. The voltage difference ΔV between parallel and anti-parallel has been observed. Typical data of spin transistor measurement is available in [28-30, 32, 33]. $\Delta V/I$ is expressed as:

$$\frac{\Delta V}{I} = P^2 \frac{\lambda_{sf}}{\sigma A} \exp(-L_{FM} / \lambda_{sf}) \qquad (1.1)$$

Where P is the Polarization rate of the ferromagnetic electrode, λ_{sf} is spin diffusion length of the aluminum film, σ is the conductivity, L_{FM} is the distance between the two ferromagnetic electrodes. In this measurement P, λ_{sf} was experimentally extracted.

The easy axes of the ferromagnetic electrodes were in the sample plane due to shape anisotropy. It was necessary to have a magnetization perpendicular to the plane in order to study the Spin Hall Effect. The relation between the magnetization direction of the electrodes and the external magnetic field was the next step of this experiment. Similar to the spin transistor measurement, the authors prepared FM1 and FM2 to be parallel and anti-parallel by manipulating the magnetic field. Then they performed similar spin transistor measurement but applying a magnetic field perpendicular to the sample plane. The magnetization of the Ferromagnetic electrodes slowly tilted out of the sample plane as the applied magnetic field increase. The injected electrons' spins precessed around an axis parallel to the applied field and projected to the detector ferromagnetic electrode. The angle θ of the magnetization to the plane was extracted from the measurement[30, 34, 35]. Sinθ, proportional to the perpendicular magnetization of one of the electodes, .is plotted as a function of the external magnetic filed, the black line in Figure 1.7d

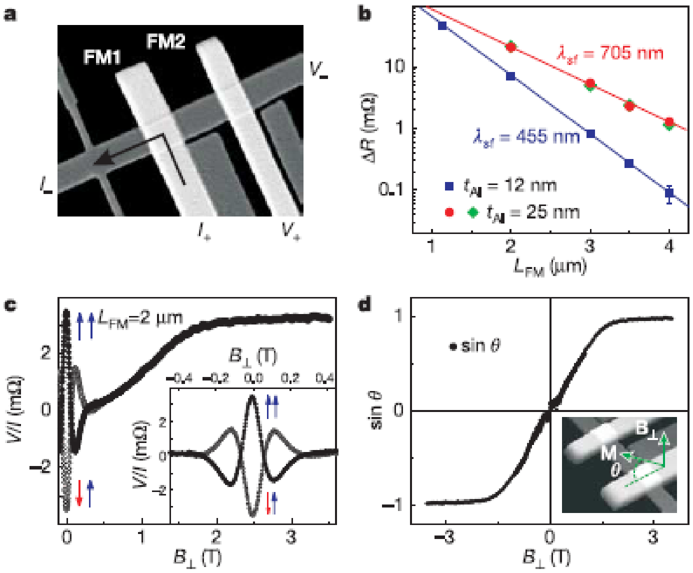

Figure 1.7 Spin transistor measurement and spin precession. a) Scanning Electron Microscopy image of the sample and measurement scheme. b) *ΔR=ΔV/I* as a function of L_{FM} c) *ΔR=ΔV/I* changes due to spin precession as a function of B⊥. d) sinθ as a function of B⊥ extracted from data in c). From Ref. 23.

.

A Spin Hall Effect measurement was performed as in Figure 1.6b. A current was injected from FM1 into the aluminum, but away from the Hall cross. The voltage on the Hall cross was measured in the presence of a perpendicular magnetic field, which was mainly used to tilt the magnetization of FM1 out of the sample plane. The measurement results are shown below in Figure 1.8.

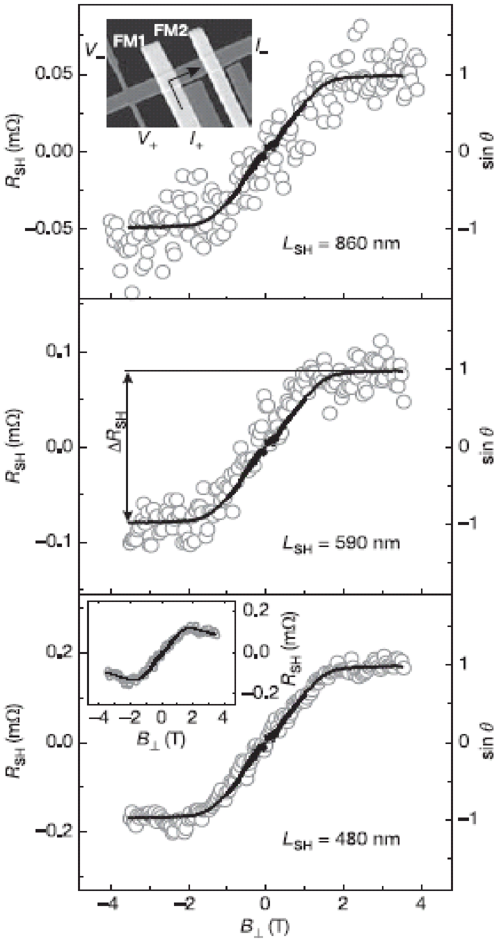

Figure 1.8 Spin Hall Effect measurements in aluminum. Three difference separation distance between FM1 electrode and the Hall cross. The V_{SH} followed the shape of sinθ, which described the out-plane component of magnetization. From ref. 23.

After the current passed FM1, the current is polarized along the magnetization direction of FM1 electrode. In the aluminum pattern, there exists an imbalance between spin-up and spin-down electrons. Some of these electrons diffuse towards the aluminum cross. The Spin Hall Effect generates V_{SH} across the two Hall cross because of the imbalanced spin up and spin down electrons. The measurement results in Figure 1.8 obey the overall shape of Sinθ as the function of the external magnetic field perpendicular to the sample plane, which is due to Spin Hall Effect.

More recently, T. Kimura and co-workers [24] reported their experiment on Spin Hall Effect in metallic system.

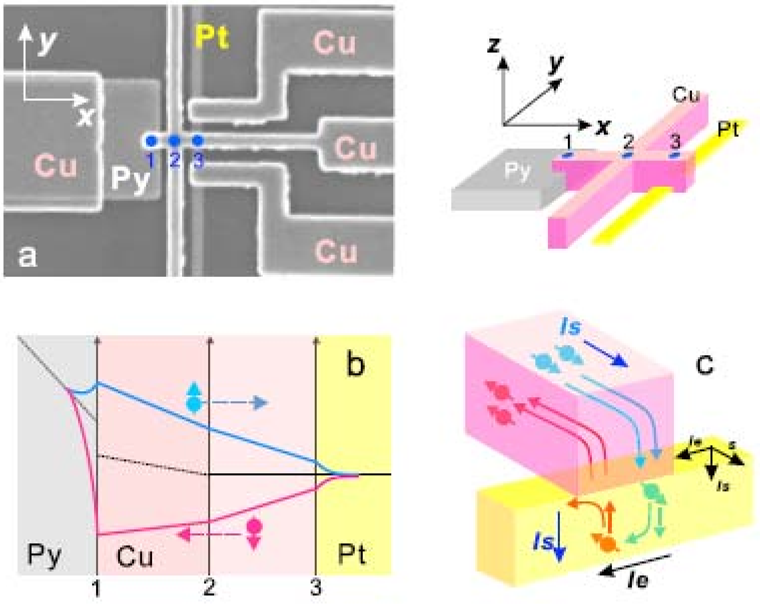

Figure 1.9 Schematic of Cu/Pt sample by Kimura. a) Scanning electron microscopy image of the device. b) Schematic spin dependent electrochemical potential map. c) Schematic illustration of the charge accumulation process in the Pt wire. From Ref. 24.

Kimura's system consists of a large permalloy (Py) pad, a thick copper (Cu) cross (100 nm by 80nm), and a thin (4nm) platinum (Pt) wire. The copper cross was 100nm wide and 80nm tickn. Figure 1.9a is the Scanning Electron Microscope image of the fabricated sample. The distance between point 1 and 3 in Figure 1.9 is 400nm, smaller than the spin diffusion length of copper at room temperature [36, 37].

When the current flows from the Permalloy electrode to one arm of the copper cross, the polarized electrons are diffused along the copper wire to the right side of the sample, and are absorbed in the thin platinum wire because of lower spin resistance in the platinum wire [36, 37]. The authors argued that a charge current $\boldsymbol{I_c}$ is generated in the Pt wire via the inverse Spin Hall Effect. The direction of $\boldsymbol{I_c}$ is given by the vector products $\boldsymbol{s} \times \boldsymbol{I_s}$ (Figure 1.9c). In the platinum wire, spin up and spin down electrons flow to the different sides of the platinum wire. When a spin current polarized along the x axis are absorbed into the Pt wire, a charge imbalance along the y axis is induced.

The measurement configuration is in the inset of Figure 1.10b. The data curve in Figure 1.10 shows that the voltage across the platinum wire depends on the direction of the permalloy magnetization, and the voltage has a hysteresis at liquid nitrogen temperature. All of these observations can be explained by the Spin Hall Effect.

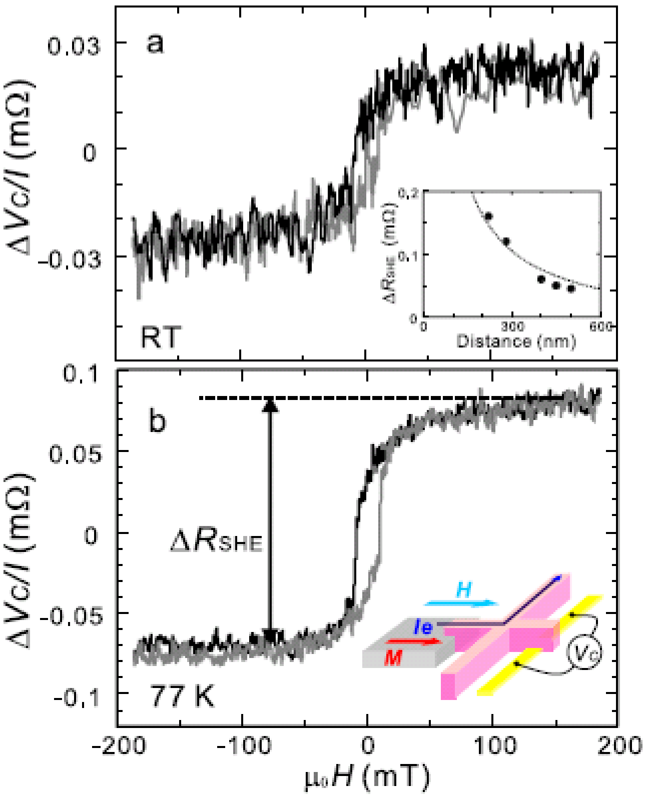

Figure 1.10 Spin Hall Effect measurement of Cu/Pt sample. a) Room temperature b) 77K. The inset of (b) shows the measurement configuration. From Ref. 24

In order to test the observed effect with the direction of the magnetization of the permalloy layer, the authors applied an in-plane magnetic field, but tilted the field direction away from the x axis in the sample plane, and measured the voltage across the Pt wire. The measurement result is shown in Figure 1.11. The voltage across the Pt wire has a cosΦ dependence, where Φ is the angle between the in-plane magnetic field and x axis. This is because $\boldsymbol{s} \times \boldsymbol{I_s}$ is not along the Pt wire. The measurement voltage is the projection of spin current, thus has a cosΦ dependence.

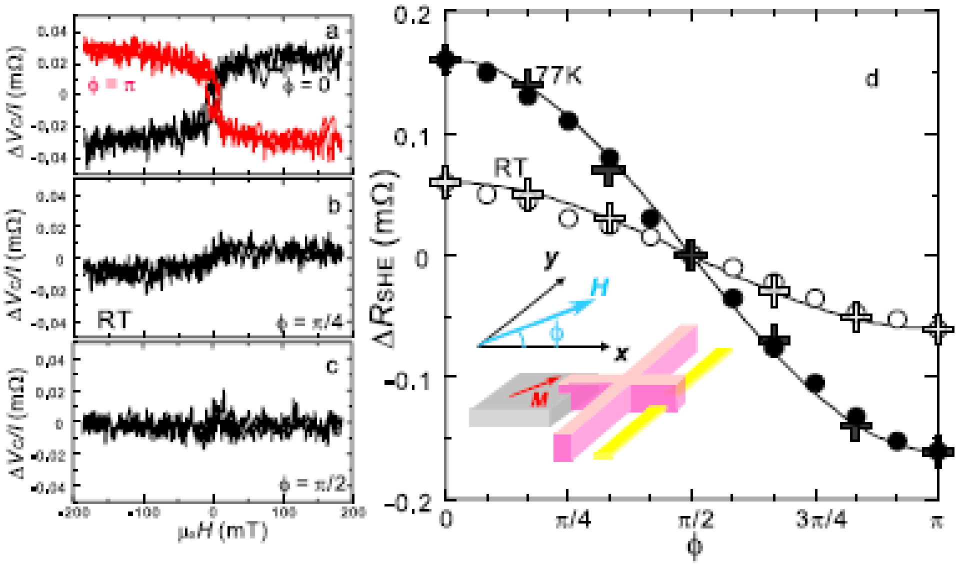

Figure 1.11 Hall resistance VS magnetic field direction. a) 0 or π, b) π/4, c) π/2. d) Overall Hall resistance change as a function of the direction of the magnetic field.

Spin Hall Effect has been extensively studied in recent years. It might provide important tools for spin injection, spin detection and spin manipulation in the design of Spintronics devices. In the following chapters, our studies of the Spin Hall Effect in metallic thin film will be presented. Our experiments started before all of the four experiments were reported. Chapter II describes some experimental techniques used in this work. Chapter III presents our experiments in micrometer size aluminum and gold thin film patterns. Chapter IV and Chapter V extend our study at nanometer size scales using a spin injection technique. Chapter covers sample fabrication, while Chapter V summarizes measurement results. Chapter VI is the conclusion.

CHAPTER II

EXPERIMENTAL TECHNIQUES

Before we present our experimental studies of Spin Hall Effect, it is useful to introduce major experimental techniques which had been employed in our experiments. Pattern generation (Photolithography and electron beam lithography), pattern transferring (etch and liftoff), thin film deposition, electroplating, and low noise electric measurements are briefly introduced. For more detailed description of these experimental techniques, please check references [38-41].

2.1 Photolithography

Photolithography is a technique that uses a light source to transfer a master pattern onto the surface of a solid material such as silicon wafer. It is a powerful tool widely used in research laboratories and in industry. It can generate features with size ranging from sub-micrometer to millimeters or even larger. Advanced photolithography in the integrated circuits (ICs) industry can create features of dimension several times smaller than the wavelength of light (currently 193nm) by using liquid immersion and a host of photomask enhancement technologies (phase-shift masks, optical proximity correction) [38]. The photolithography process involves photoresist application, soft baking, mask alignment, exposure, development, and hard-baking (optional).

2.1.1 Substrate preparation

We start with a small piece of silicon diced from a commercial silicon wafer. Our measurement is at four Kelvin the intrinsic carriers' density of the silicone is negligible. It is safe to consider the substrate is an insulator at low temperature. The wafer piece is soaked in an acetone bath with ultrasonic agitation for about 15 minutes. Then the wafer is rinsed with acetone and isopropanol sequentially, and dried with nitrogen gas or spin dried. The substrate is baked on a hot plate at 160 degree Celsius for about 10 minutes to remove solvent accumulated from the cleaning process. This cleaning process is crucial since any dust left on the substrate may result in defects in the final patterns.

After the wafer is cooled down to room temperature, photoresist (Shipley 1805 in this study) is applied onto the substrate with a pipette, and the substrate is spun rapidly to produce a uniform photoresist layer using a spin coater. The thickness of the photoresist depends on the spinning speed and viscosity of the photoresist. The empirical expression for the thickness t is given by:

$$t = \frac{KC^{\beta}\eta^{\gamma}}{\varpi^{\alpha}} \tag{2.1}$$

where *K* is the overall calibration constant, *C* is the polymer concentration in g/100ml solution, η is the intrinsic viscosity, ω is the rotation speed (rpm). For Shipley 1805, a spinning speed of 3000 rpm produces a resist layer of 500nm in thickness. The substrate with photoresist is baked on a hot plate with temperature set at 115℃ for about 30 minutes to remove solvent in the photoresist, which is called soft bake. The photoresist is ready for the next step--exposure. In industry, the whole wafer is processed and then sliced into small pieces to package. In our facility, we don't have this capability.

2.1.2 Photoresist exposure

There are two types of photoresist: positive and negative. For a positive photoresist, exposure to the Ultraviolet (UV) light changes the chemical structure of the resist so that it becomes more soluble to a certain developer solution. The resist exposed by the UV light is then washed away by the developer solution. A negative photoresist behaves in just the opposite manner. Exposure to the UV light causes the negative resist to polymerize. The developer solution removes only the unexposed negative photoresist. Therefore, the negative resist exposed by the UV light remains on the substrate. Figure 2.1 shows a schematic patterning process for positive and negative photoresist.

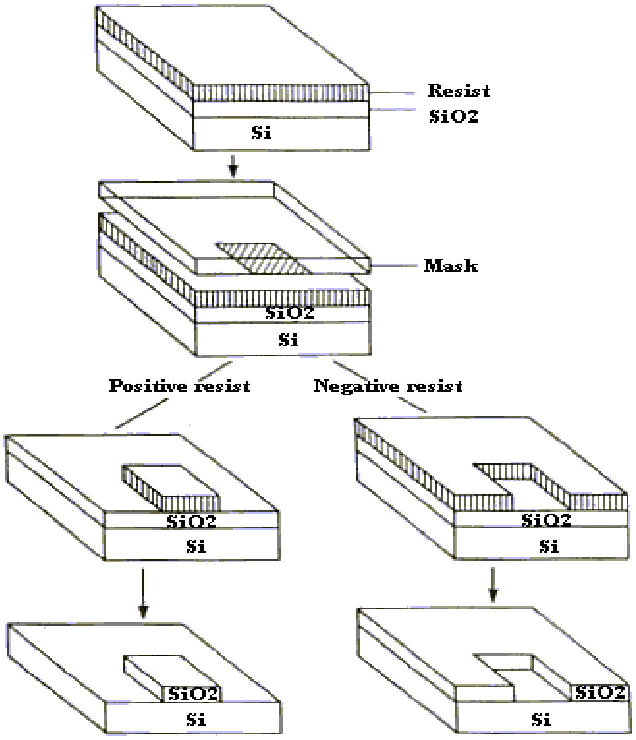

Figure 2.1 Illustration of photolithography patterning process

The photolithography process transfers the pattern on the photomask to the photoresist. The pattern on the photomask is created in a similar lithographic way. On a fused quartz, a thin chrome layer is first deposited. Then a resist pattern is created on the chrome by a Laser Plotter[42] or electron beam lithography. The chrome film without photoresist protection is etched away while the chrome underneath the resist is protected. Then the photoresist is stripped and a chrome pattern is left. Light is blocked by the remaining chrome layer and passes through the quartz glass so that the chrome pattern allows selective light pass. Depending on the gap between photomask and the substrate, the photolithography can be classified as direct print and project printing. In our system, the mask is in direct contact with the photoresist layer, and transfers a 1:1 image of the pattern on the mask onto the silicon wafer.

In photolithography, the exposure time, exposure light density, development time, photoresist baking time and baking temperature are the main parameters that have to be optimized to fabricate good patterns with high yield. Advanced photolithography requires much more complicated process, more sophisticated equipments, and advanced computer modeling and control. Using photolithography, engineers in major semiconductor companies are able to create features as small as 30nm! For research labs, most researchers have to use other techniques to create nanometer size features. Electron beam lithography is one of the popular techniques.

2.2 Electron beam lithography

Our photolithography system can create features down to 2 μm in direct contact mode, limited primarily by the feature size on the photomask. To fabricate samples with smaller features, electron beam lithography (EBL) is frequently used.

EBL works similar to Photolithography. It uses high-energy electrons beam to expose the resist layer rather than using UV light in the Photolithography process. This is a very powerful and flexible tool to create nanometer size patterns without using masks which are usually expensive. In industry, EBL is mainly used to generate photolithography masks or for low volume production.

EBL mainly consists of an electron source that can produce an electron beam and a beam blanker that can turn the electron beam on and off. The electron beam is focused by one or two condenser lenses into a beam with a very fine focal spot ranging from 1nm to 5nm in diameter. The electron beam passes through pairs of scanning coils in the objective lens, which can move the beam in both horizontal and vertical directions. The beam blanker consist a pair of parallel plates where the electron beam passes through. When a voltage (100 volts) is applied between the two plates, the electron beam is deflected to the plates due to the electric force by the strong electric field generated by the voltage. The beam is off from the substrate point of view. If zero voltage is between the plates, the electron beam can pass through the plates. The beam is on. The beam is directed to specific positions on the surface by the scanning coil and the beam is turned on where the resist is to be exposed. A computer controls this writing process. The electron beam lithography patterning process does not need any masks. The pattern is directly controlled by a computer with proper software.

EBL offers higher patterning resolution than optical lithography because of the shorter wavelength of higher energy electrons used in the process. The wavelength of the electron is given by the de Broglie equation, if neglect the relativity effect,

$$\lambda = \frac{h}{p} = \frac{h}{\sqrt{2m_e eV}} \tag{2.2}$$

where h is Planck's constant, p is the momentum of the electron, m_e is the mass of electrons, e is the elementary charge, and V is the accelerating voltage. The acceleration voltage we used is 30kV, which gives a wavelength of about $7*10^{-12}$m.

However it takes longer to write a pattern using electron beam lithography. The resist pattern is created in a 'serial' manner, making it slow compared to optical lithography where patterns are generated in a 'parallel' way. The electron beam has to be well optimized in order to create nanometer size patterns. Optimization is a very complicated process. Due to the complexity of the technique, operational details are presented below.

A substrate is first cleaned according to the protocol presented in Section 2.1. A pipette is used to place a few drops of liquid of 950K (Monochlorobenzene, 3%) PMMA (polymethyl methacrylate) onto the substrate. The substrate with PMMA is then spun by a spin coater. The spinning speed determines the thickness of PMMA layer. The PMMA is manually scratched near the edges of the sample using a sharp object, e.g. sharp tip of tweezers, for a coarse focus adjustment.

The prepared sample is mounted onto the sample stage of a SEM (JEOL-JSM6460). To prevent charging effect, a metal clip is used to firmly press the sample to the stage. The chamber is pumped down until the internal vacuum gauge detects a low enough pressure indicated by the system. After pumping for another 10 min, the filament is turned on with an accelerating voltage of 30KV. A Faraday cup is used to saturate the filament and to optimize the electron beam. The beam is moved to the Faraday cup by moving the sample stage and increasing the magnification until the beam is fully within the Faraday cup. The filament current is increased slowly by clicking the current bar on the SEM control screen. The beam current is measured with a Keithley 6485 Pico-ammeter. Figure 2.2 shows the saturation process in our system. As the filament current increases, a false peak appears first. The filament current is continually increased. In this saturation process, the change of beam current between each click of the filament current bar is closely monitored. It is important to record the highest change of beam current between two clicks. When the change of beam current between two clicks is about a quarter of the highest beam current change, the filament is saturated properly. The filament saturation is extremely important. If the filament current is too low, the electron beam is not stable and easily affected by other settings. If the filament current is too high, the lifetime of the filament decreases dramatically.

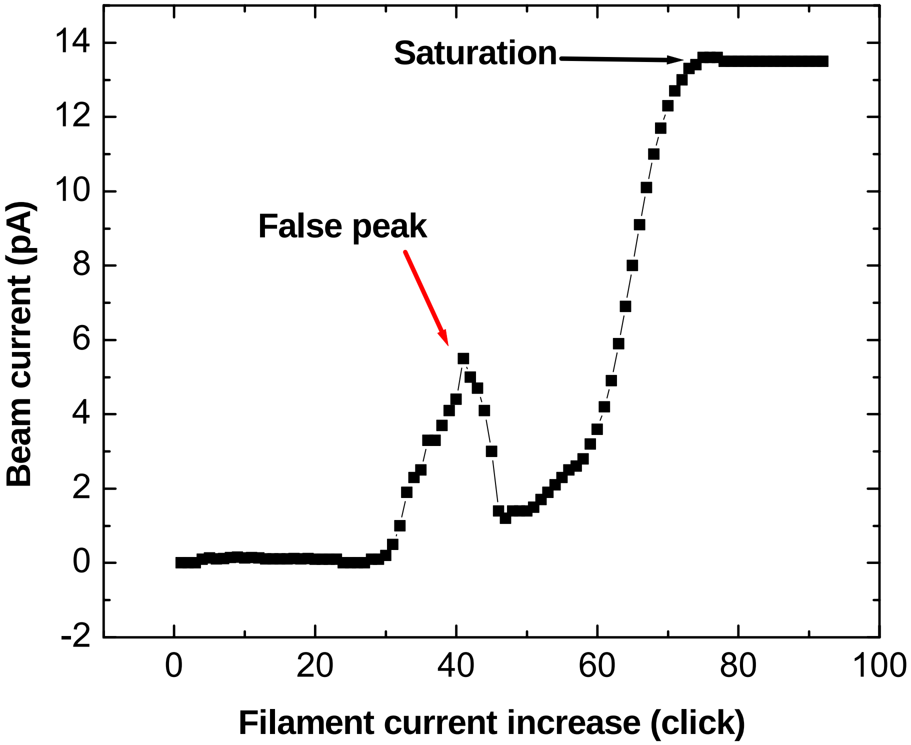

Figure 2.2 Beam current VS filament current during filament saturation

To optimize the electron beam, the tilt and shift of the electron beam is iteratively adjusted at a smaller (~25) and bigger (~90) spot size respectively after the electron beam is turned on for at least 10 minutes. In the ideal case, the beam current is maximized and observed to be symmetric in both tilt and shift. In the writing process, different beam currents might be used if the patterns have various dimensions. The Faraday cup is used to find the corresponding spot size for different beam currents. Large beam current (large spot size) is used to write bigger patterns. Small beam current (small spot size) is used to write fine features. It takes more effort to optimize the EBL system to write small features. The optimization process is conducted in small beam current because the system requirements to write bigger patterns are loose. Once the system is optimization to write small features, it can generate bigger features as long as the dosage is set properly.

The optimized electron beam is moved to a gold standard to adjust focus and stigmatism. The focus and stigmatism is iteratively adjusted to get a better image of gold grains. This procedure is performed at several magnifications until gold grains are clearly resolved. Once a clear gold picture is observed, the wobbling is checked. In this step, a smaller separate square showing a real-time scan image is compared to a frozen image. Two external knobs are used to minimize the movement of the scanning image in horizontal and vertical directions. The adjustment of focus, stigmatism and wobbling is repeated until a clear edge of gold grains is observed, Figure2.3. The gold standard is mounted about the same height as the sample. Usually the fine focus is adjusted in the following operation. The stigmatism is usually not changed after this step. For experienced operators, the stigmatism may be carefully adjusted on contamination spots to achieve better patterning result.

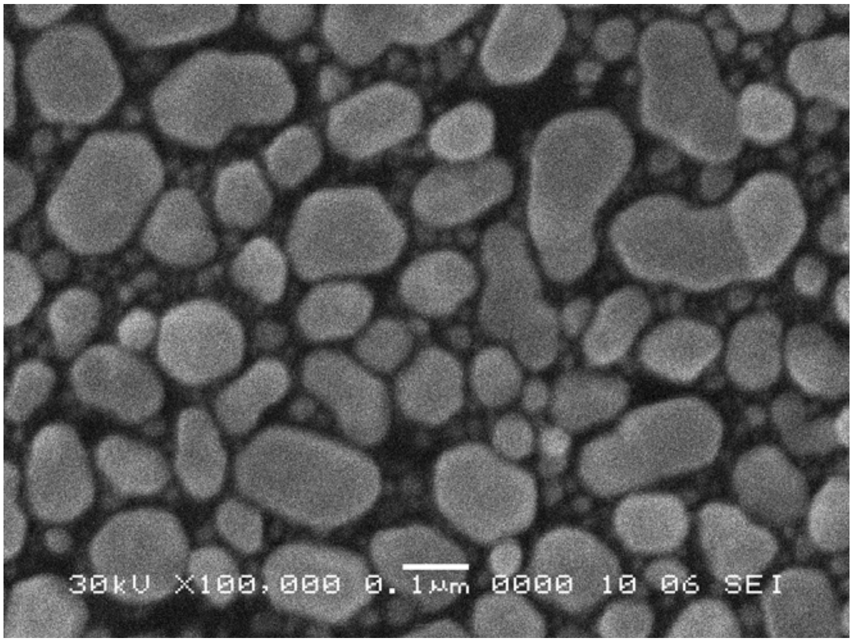

Figure 2.3 SEM image of a gold standard sample scanned at X100,000

It is necessary to move the electron beam back to the Faraday cup to check the filament saturation and beam alignment. The beam current might increase after optimization depending on previous conditions. If any adjustment such as filament saturation current, tilt or shift is made again, the adjustment of focus and stigmatism has to be repeated. After the optimization is finished, the electron beam is carefully moved to the edge of the sample to locate the scratch, and focuses at the end of the scratch, Figure 2.4.

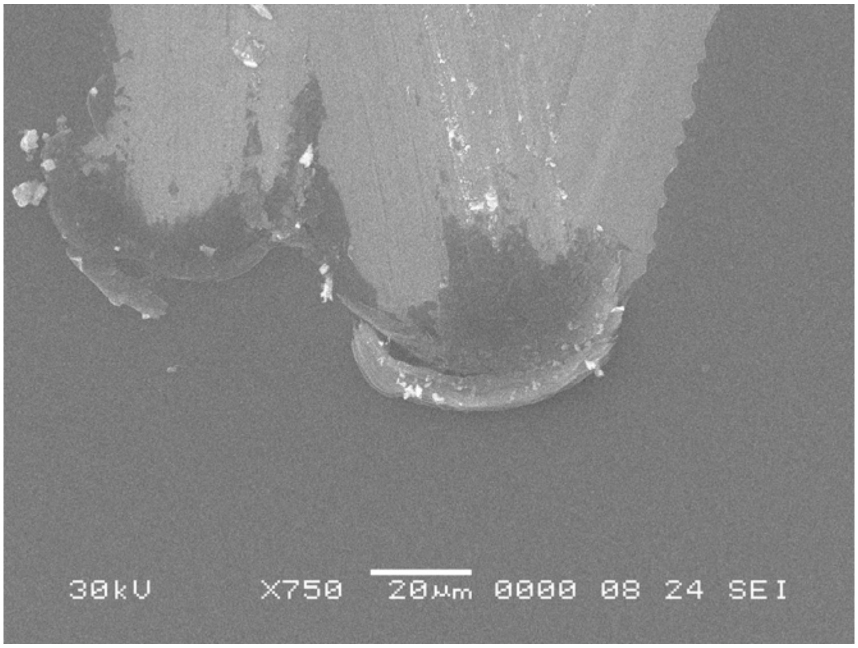

Figure 2.4 SEM image of the end of a scratch on the PMMA

Focus on the scratch is important because the sample is usually a few millimeters away from the gold standard and may have slight difference in height so that refocus might be necessary. Focus on the scratch brings focus as close as possible to the final focus of actual E-beam writing.

After adjusting the focus on the tip of the scratch, the beam is moved 20µm towards the center of the substrate with the beam off. The system is switched to writing mode. The electron beam is turned on and the PMMA is exposed. If the electron beam is well optimized and properly focused, the beam current reading from the Pico-ammeter decreases with time as the increase of the back scattered electrons reduces the total current of the electron beam. The system is switched to scanning mode. At the center of the screen, a round, uniform dot is observed if the system is properly optimized, Figure 2.5. It might be difficult to create a small and round contamination spot at the first time. Focus and stigmatism may be adjusted on the contamination spot. The contamination spot creating process is repeated until a nice, round, uniform dot is observed.

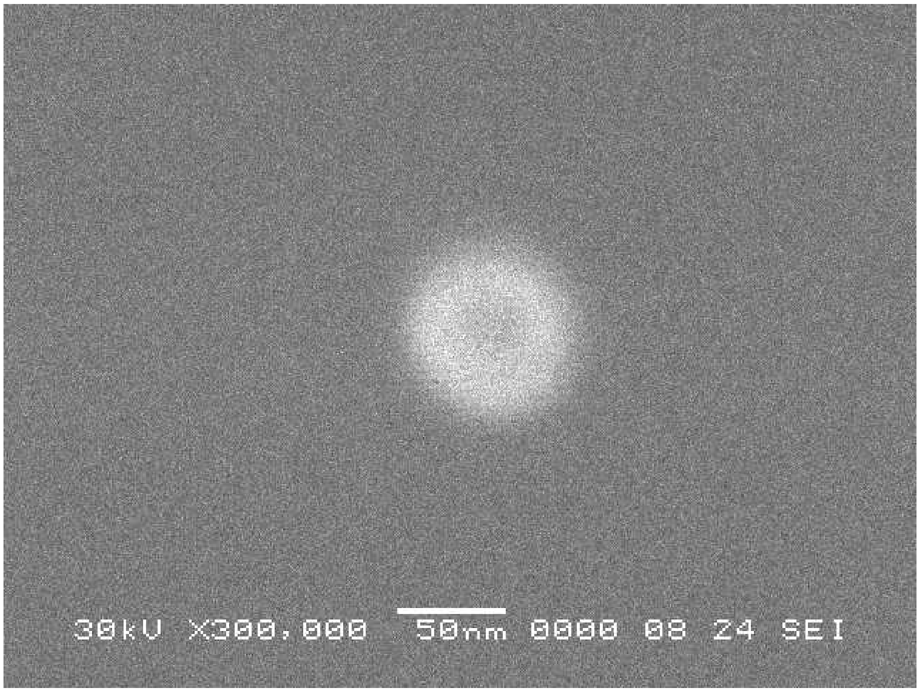

Figure 2.5 SEM image of a contamination spot. The PMMA surface was exposed by an optimized electron beam.

After the optimization process is completed, the system is ready to write patterns. The system is switched to writing mode. The electron beam is on beam blanking mode. The run file created by a NPGS software is processed to create nanometer size patterns.

2.3 Pattern transferring

Once the pattern is generated by either Photolithography or electron beam lithography on a resist, it is necessary to transfer the pattern onto the silicon wafer. There are two ways to transfer the resist pattern: etch, or lift off, Figure 2.6 and Figure 2.7. In the etch process, a thin film is deposited first before the resist patterning. After lithographic process, part of the film is covered by the resist pattern while the rest is unprotected. A dry/wet etch technique is then used to remove the unprotected film. The resist patterns protect the material underneath. The thin film pattern appears after the resist is removed. This dry/wet etch method is widely used in semiconductor business to make integrated circuit on Silicon. In the liftoff process, a thin film is deposited after the lithographic patterning. The sample then is immersed in some chemical (acetone in our experiments). The film that makes direct contact with the substrate stays while the film on top of the resist pattern is removed.

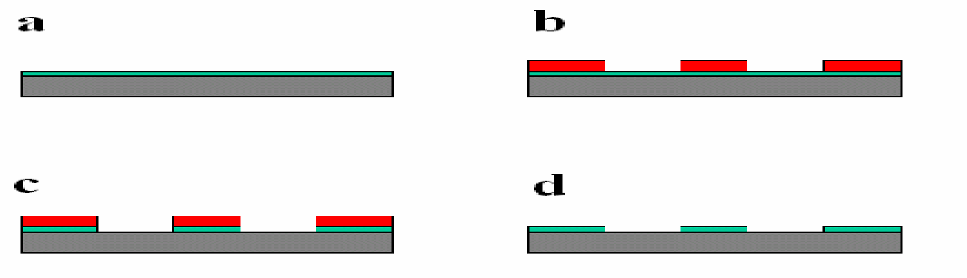

Figure 2.6 Illustration of etch process. a) Deposit thin film. b) Pattern photoresist. c) Etch film using resist as protective mask. d) Remove resist to get pattern.

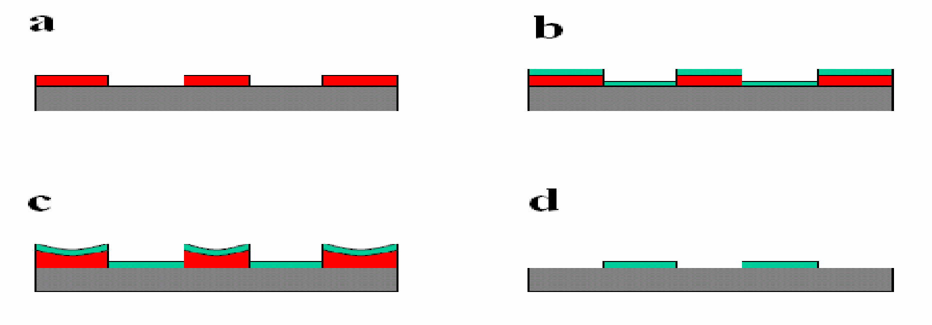

Figure 2.7 Illustration of liftoff process. a) Pattern photoresist. b) Deposit thin film. c) Soak the sample in a solvent which can remove the resist. d) Clean and dry sample

2.4 Thin film deposition

In Section 2.2, a thin film is deposited either in etch or liftoff process. There are many techniques for deposition: thermal evaporation, electron gun deposition, sputtering, chemical vapor deposition, and so on. The photoresist and PMMA are sensitive to temperatures. At high temperature, resist will degrade and is difficult to remove afterwards. If high temperature is required for the material growth, dry/wet etch method is usually used to transfer patterns.

The thin film used in our experiments is deposited by thermal evaporation. The source material is loaded into a tungsten basket or tungsten boat. After pumping to a high vacuum ($5*10^{-6}$torr) using a diffusion pump, the tungsten basket/boat is heated with an electric current. The temperature of the source material is raised to exceed the melting point. The vapor of the material radiates and forms thin film when it hits the substrate.

A Quartz Crystal Microbalance (QCM) is used to monitor the evaporation rate and measure the film thickness. The QCM sensor head is placed near the sample. When the material vapors deposit on the quartz crystal, the mass of the quartz crystal changes. The resonant vibration frequency of the piezoelectric quartz crystal has a correlation with the mass, known as Sauerbrey equation[43]

$$\Delta f = \frac{-2\Delta m {f_0}^2}{A\sqrt{\rho_q \mu_q}} = -C * t \tag{2.3}$$

where, f_0 is the resonant frequency of the crystal, A is the active area of the crystal (between the electrodes), ρ_q is the density of quartz (2.648 g/cm^3) and μ_q is the shear modulus of quartz (2.947*10^{11}g/cm.s^2). Δm is the change of mass on the quartz crystal due to the deposited material, and linearly depends on the film thickness t. The frequency is measured by a frequency counter with high acuracy. The constant C is calculated from the equation, and is adjusted by measuring the thickness of deposited film using a Dektak profilometer. The Sauerbrey equation holds near f_0. If the frequency reading is off by 10% after some use, the quartz crystal should be changed.

2.5 Electroplating

Electroplating is a process of using an electrochemical reaction to grow a layer of metal onto a conductive surface in a solution. The surface to be plated is connected to a negative potential, making it a cathode as in Figure 2.8. When there is a voltage between the cathode and the anode, the cathode attracts positive ions in the solution. These ions receive electrons from the cathode and form atomic layer onto the surface. The anode can be made of the material to be electroplated. In this case, the anode slowly dissolves and replenishes the ions in the solution. A nonconsumable anode such as lead, platinum, or graphite can also be used. In the latter case, the metal ions in the solution must be periodically replenished in the bath as they are drawn out of the solution continously.

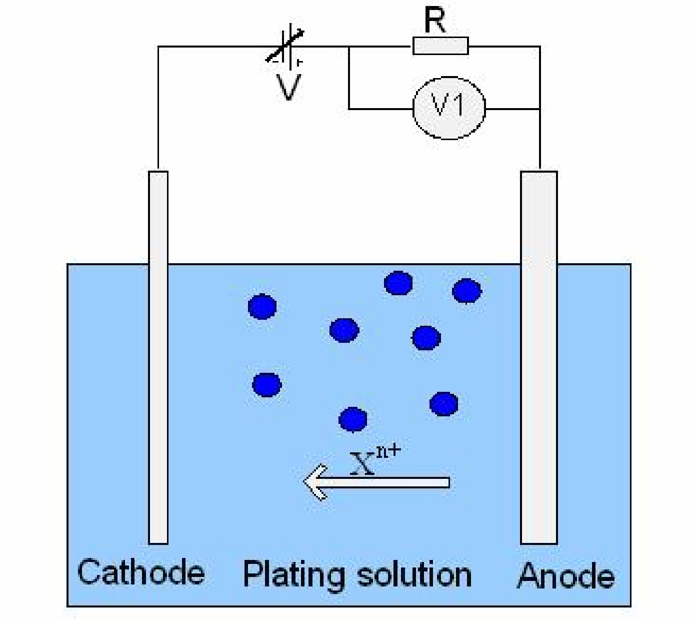

Figure 2.8 Schematic of an electroplating process

The electroplating speed depends on the efficiency of the anode and cathode, the electrolyte, and the electroplating current. If growth on certain area of the cathode is not desired, tape or foil is used to prevent the solution from reaching the area.

In our experiment, we want to electroplate through a PMMA pattern. The PMMA pattern is on top of a metal thin film patterns. The film pattern is connected as a cathode. The electroplating process only occurs at the places where the metal film is exposed to the plating solution. More details about the experiment is presented in Chapter IV.

Single element material electroplating is straightforward. Alloy electroplating is more difficult and usually is achieved by selecting proper electrolyte and the ratio of element is controlled by electroplating current density.

2.6 Low noise electric measurement

Low noise electric measurements[39, 40] are very important in this study. We need to measure electric properties of micrometer and nanometer size patterns. The signal is in the order of 10^{-9} volt, which is comparable to the thermal noise.

A lock-in amplifier can pick up low-level signals from a noisy environment, and is useful in this work. Operation of a lock-in amplifier relies on the orthogonality of trigonometric functions. Specifically, when a trigonometric function of frequency f_1 is multiplied to another trigonometric function of frequency f_2 not equal to f_1 and integrated over a time much longer than the period of these two functions, then the result is zero. When f_1 is equal to f_2, and the two functions are in phase, the average value is equal to half of the product of the amplitudes. Lock-in amplifier picks up signals with particular frequency only. Any signal with a different frequency is attenuated. The relative phase of the signal with respect to reference signal can be measured. To increase the measurement sensitivity, the output of the lock-in amplifier is fed into the input of a Keithley multimeter. The readings of the Keithley multimeter is taken by a labview program for four minutes for each measurement. The computer accquired data is averaged, and has measurement sensitivities as low as a few nanovolt.

For small signals, electrostatic coupling or interference might change the measurement results significantly. Electrostatic coupling or interference occurs when an electrically charged object is brought close to an uncharged object. It could produce noisy or erroneous reading. The following steps can reduce this effect: 1. keeping all charged objects (including people) away from sensitive areas of the test circuit. 2. Avoiding movement and vibration near the test area. 3. Using good quality coaxial or triaxial cables to make connections and properly shielding the devices being tested. 4. Grounding properly to avoid ground loop.

Due to space limit, the above techniques are briefly presented. In the next two chapters, we will show how these experimental techniques are used in our experiments and more experimental details are covered.

CHAPTER III

SPIN HALL EFFECT IN MICROSCOPIC SAMPLES

From the introduction in Chapter I, if an electric current flows in a system, a spin current is generated perpendicular to the current flowing direction due to Spin Hall Effect. In a paramagnetic system, on the two sides of the current path, there is a spin imbalance, but no charge imbalance because of the equal number of spin up and spin down charge carriers. To detect this spin imbalance is a difficult task. Currently available magnetometers do not have the sensitivity needed to measure the small local magnetization of the imbalanced spins in metallic systems. In this chapter, we will present our experimental effort in micrometer size samples.

3.1 Proposed experiment in aluminum by Hirsch

Spin Hall Effect was first proposed over thirty years ago, and more recently revived by Hirsch [14]. In his paper [14], Hirsch proposed an experimental scheme to detect the Spin Hall Effect. Hirsch suggested a three-layer-system (Figure 3.1) in analogy to a Double Hall Effect device [14]. The first and third layers are conductors, separated by a thin insulating layer. On the two sides of the insulating layer, two small windows patterned by photolithography are etched in order to make contacts between the first and third conducting layers. In the presence of a magnetic field, there is an ordinary hall voltage across the two edges of the bottom strip due to the Lorentz force. Since the top conductor connects the bottom conductor through two contacts, a current induced by the ordinary hall voltage circulates in the top conductor. This current is proportional to the external magnetic field B. The induced current is also affected by the external magnetic field so that ordinary hall voltage across Point 1 and 2 in Figure 3.1 is proportional to B^2. This effect is called Double Hall Effect.

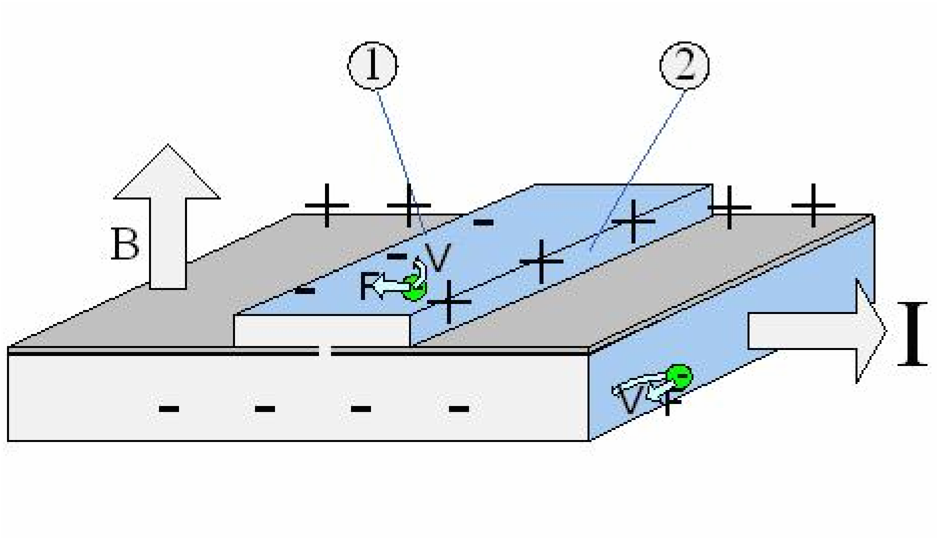

Figure 3.1 A Tri-layer structure exhibits Double Hall Effect. The top strip is insulated from the underneath current carrying layer except two contact points at the two edges. In a magnetic field, Double Hall Effect exists between points 1 and 2 in the top conducting layer.

Hirsch argued that a Spin Hall Effect could be detected in the above proposed system. From the theory of Spin Hall Effect, in the bottom layer, spin up electrons are preferentially deflected to left (or right), while spin down electrons are deflected to right (or left). Some of the electrons pass through the two contacts and diffuse into the top layer (Figure 3.2). The same mechanism that deflects electrons' spins in the bottom layer exists in the top layer. Therefore, spin up electrons are deflected to the left (point 1 side). For spin down electrons, they are deflected to the right. Both spin up and spin down electrons are deflected to the same side in the top layer and a charge imbalance is established on the two sides of the top layer. This voltage is a direct evidence of Spin Hall Effect.

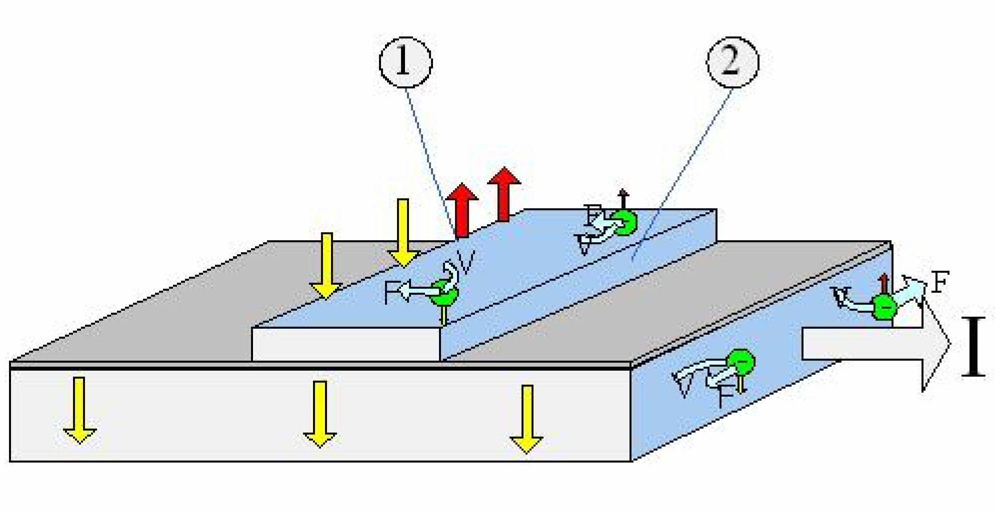

Figure 3.2 Spin Hall Effect in tri-layer structure. Spin up and spin down electrons are preferentially deflected to different sides in the bottom conductor. The accumulated spin up and spin down electrons diffuse into the top layer through the contacts. The same mechanism defects spin up and spin down electrons to the same side.

Hirsch calculated the effect and obtained the following equation to estimate the Spin Hall Effect:

$$V_{sc} = \frac{8\pi^2 R_{s1}^{\;2} R_{s2}^{\;2} n_1 n_2 \mu_B^{\;2} j_x l}{\rho_2} \tag{3.1}$$

where $R_{s1,} R_{s2}$ is the anomalous Hall coefficient of the bottom and top conductor, $n_{1,} n_2$ is the carriers' density of the bottom and top conductor, μ_B is the Bohr magneto, j_x is the current density in the bottom layer, l is the width of the top conductor, ρ_2 is the resistivity of the top conductor. In a simple case where the top and bottom conductors are made from the same material, the equation simplifies

$$V_{sc} = \frac{8\pi^2 R_s^{\;2} n^2 \mu_B^{\;2} j_x l}{\rho} \tag{3.2}$$

For aluminum, if $Rs=R_0=3.45*10^{-11}$m^3/C, l=100μm, $j_x=6*10^6$A/m^2, $\rho=2.7*10^{-3}$μΩ cm, V_{sc} is estimated as 58nv, measurable in most laboratories.

In the presence of a magnetic field, there is an additional term from the Double Hall Effect

$$V(B) = \frac{(R_0^{\;2} B^2 + R_s^{\;2} B_{eq}^{\;2}) l j_x}{\rho} \tag{3.3}$$

It may be difficult to measure the Spin Hall Effect at zero magnetic field. However, it is possible to extract the Spin Hall Effect from the extrapolation of results for *V(*B*)* to *V*(B=0)

3.2 Our experiment

Hirsch proposed a possible system for experimentalist. However from an experimental point of view, alignment and interface resistance are big issues to prepare the device suggested by Hirsch. In order to solve these two issues, we improved the sample geometry as in Figure 3.3 which eliminates the above difficulties.

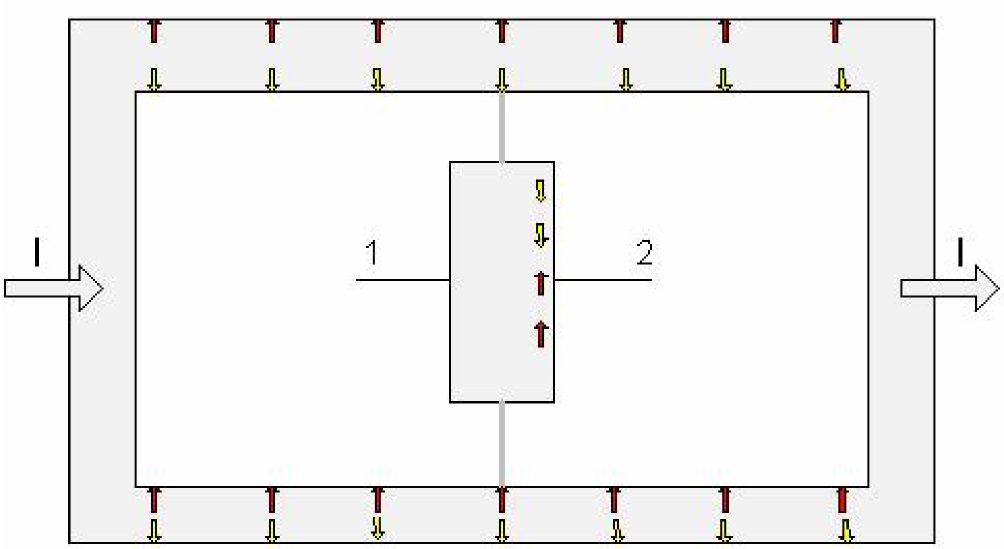

Figure 3.3 Schematic of an improved device to study Spin Hall Effect

In this device, a current is carried in two identical parallel strips which are connected by a cross transverse strip, made of the same material. This new designed samples can be fabricated in one step lithography patterning. No alignment is needed during sample fabrication. The alignment issue is taken care of during the photolithography mask designing and fabrication. Furthermore, there is no interface problem due to the single layer. In each of the two parallel strips, the Spin Hall Effect leads to a separation of spins on opposite sides of the strip. Therefore, the “inner” sides of the parallel strips, which are facing each other, accumulate majority spin populations of opposing spins. The “inner” sides are connected with a transverse strip, as shown in Figure 3.3, which allows spins to diffuse through. Similar to Hirsch’s theory, the same spin dependent perpendicular force, which leads to the spin separation in the 2 parallel current-carrying strips, deflects either spin population to the same side of the transverse strip, leading to an electric voltage between point 1 and 2 in Figure 3.3. This voltage is a signature of the Spin Hall Effect.

In the presence of a perpendicular magnetic field B, an ordinary hall voltage across the 2 parallel stripes causes charge current to flow across the transverse strip and gives another contribution to the voltage between point 1 and 2. This Double Hall Effect is proportional to B^2. Figure 3.4 shows the schematic drawing of a sample. To simplify the description, we label the contact pads with numbers. In the measurement, we choose pad 11 as I+ and pad 1 as I-. 12 pads on the sample enable us to check consistency between various pads. In addition, electrical resistivity, hall coefficient and spin hall voltage are measured in one sample. We expect a voltage between points 1 and 2 in Figure 3.3 due to Spin Hall Effect, and B^2 dependence due to the Double Hall Effect.

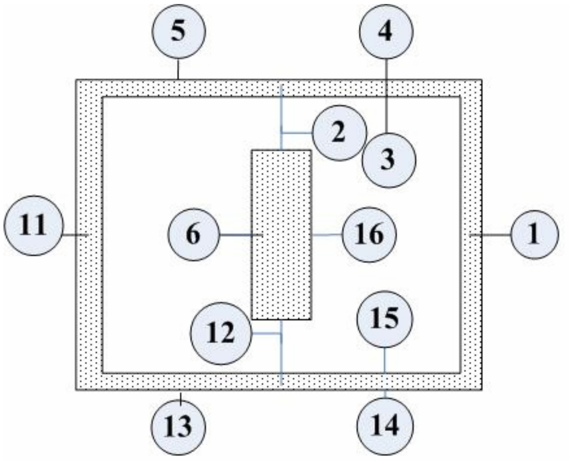

Figure 3.4 Schematic of Spin Hall Effect sample and pads coding for simplicity

3.2.1 Experimental work in aluminum

Aluminum is the material suggested by Hirsch. The reason to choose aluminum is that aluminum has large spin diffusion length. Johnson[31] measured the spin diffusion length of aluminum δ_s~450μm at T=4.3k and δ_s~170μm at room temperature.

Aluminum samples were made by photolithography and liftoff techniques as introduced in Chapter II. We used positive photoresist (Shipley 1805) in our fabrication process. The photoresist was spin coated onto a clean silicon wafer at 3000rpm for 60 seconds, then soft baked on a hot plate at 115 degree Celsius for 30 minutes to remove solvent in the photoresist. After the resist was cooled down, it was exposed to a UV light for 3 seconds at energy density of 1.7 mW/cm^2 using a mask aligner. The exposed resist was developed in MF-319 solution for 60 seconds and rinsed with deionized water thoroughly. These parameters are optimized to have a yield of about 85%.

To transfer the photoresist pattern, we used thermal evaporation and liftoff techniques. A thin aluminum film was thermally evaporated at high vacuum. The thin aluminum film covered the entire photoresist pattern. In the liftoff process, aluminum on top of the photoresist was removed by acetone, whereas aluminum that made direct contact to the silicon substrate stayed. The aluminum film was evaporated at a pressure of 5*10^{-6}torr. The evaporation rate was about 3Å/second. The thickness of the aluminum film was about 20nm. The sample was cooled down to 4.2K and measured with a PAR 124 lock-in amplifier and a PAR 113 preamplifier. Various measurement results were presented in the following paragraphs.

A voltage along the current strip between pads 5 and 4 was measured in the presence of a magnetic filed. The magnetic field is perpendicular to the sample plane. Positive field meant the field goes into the sample. The voltage with magnetic field is shown in Figure 3.5. Measurement current is 1μA. From the data, the longitudinal resistance exhibits a magnetic dependence. This magnetoresistance of aluminum, consistent with literature, is not the focus in this work. But this magnetoresistance may add an additional term to our measurement of Spin Hall Effect or Double Hall Effect.

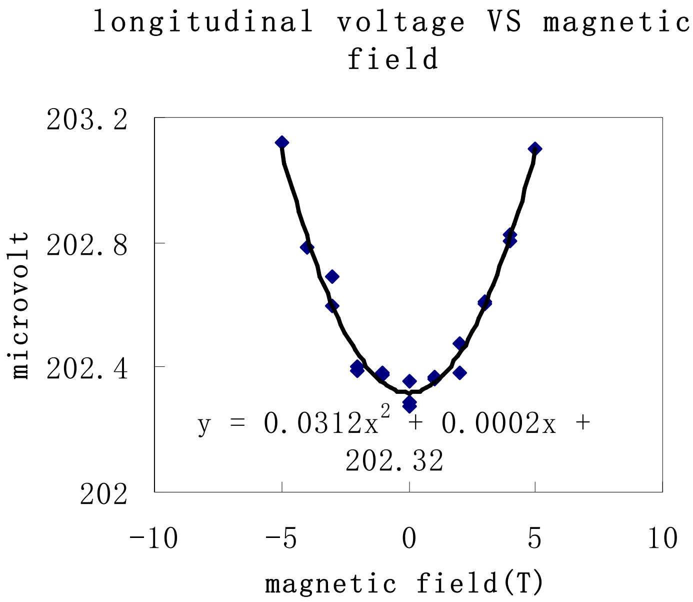

Figure 3.5 Longitudinal measurement of aluminum sample in magnetic field with measurement current of 1μA.

The resistivity of the aluminum thin film can be calculated from the geometry. For the longitude voltage measurement, the length L of the current strip between pads 5 and 4 is 1390μm; the width W of the current strip is 20μm. Electric resistivity is calculated from the following equations:

$$R = \frac{V}{I} \tag{3.4}$$

$$R = \frac{\rho L}{Wt} \tag{3.5}$$

From equations (3.4) and (3.5), ρ is obtained as:

$$\rho = \frac{VWt}{IL} \tag{3.6}$$

where V is the voltage drop between pads 5 and 4, W is the width of the current strip, t is the thickness of the aluminum film, I is the current in the strip, and L is the length of the current strip that is measured. The resistivity is obtained as:

$$\rho = \frac{202 * 10^{-6} * 20 * 10^{-6} * 20 * 10^{-10}}{0.5 * 10^{-6} * 1390 * 10^{-6}} = 1.16 * 10^{-8}\Omega \bullet \mathrm{m} \tag{3.7}$$

We have obtained the electric resistivity for 20 nm thick aluminum film ρ(20nm) is $1.16*10^{-8}\Omega\bullet$m at 4.2k. The conductivity of the aluminum film σ(20nm) is $8.6*10^{7}\Omega^{-1}\bullet$m^{-1} is bigger than $1.7*10^{7}\Omega^{-1}\bullet$m^{-1} in [23]. The conductivity difference between our value and [23] is possibly due to the dimension difference. Our sample has a width of 20μm, while the system in [23] is about a few hundred nanometer. Our system might have less surface scattering due to larger dimension, and gives larger conductivity.

Several pairs of electrodes among the 12 contact pads locate on the two current paths, which make it possible to measure Ordinary Hall Effect at different locations of the current paths. For every pair on the current path we observed similar linear dependence with external magnetic field. We randomly select the Ordinary Hall Effect measurement between pads 15 and 14 and present the result in Figure 3.6.

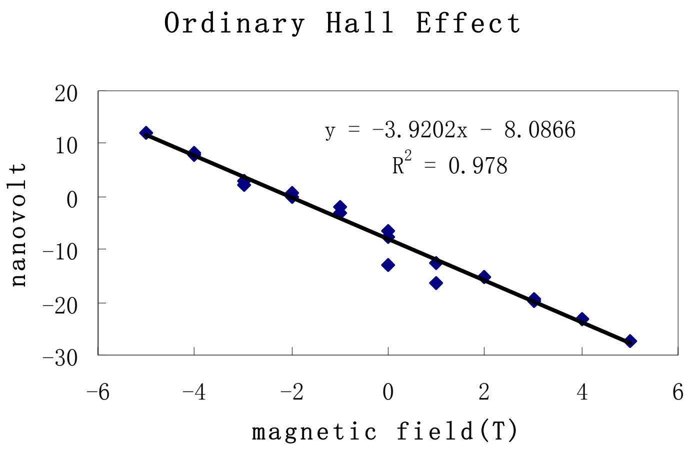

Figure 3.6 Ordinary Hall Effect of an aluminum sample. The voltage was measured between pads 15 and 14 with measurement current of 10μA.

The Ordinary Hall voltage was measured between pads 15(voltage +) and 14(voltage -) in the presence of magnetic field. The magnetic field is perpendicular to the sample, and the positive field means the field goes into the sample plane. The measurement current is 10μA. From the direction of the slope, we conclude that charge carriers are electrons in aluminum film. From the magnitude of the slope, we obtain Hall coefficient(R_0) $1.56*10^{-11}$ $m^3amp^{-1}sec^{-1}$ at 4.2K, which is consistent with values in literatures[19].

We expect a Spin Hall Effect and Double Hall Effect in our system. We measured the voltage between pads 6 and 16 in magnetic field. The result is shown in Figure 3.7.

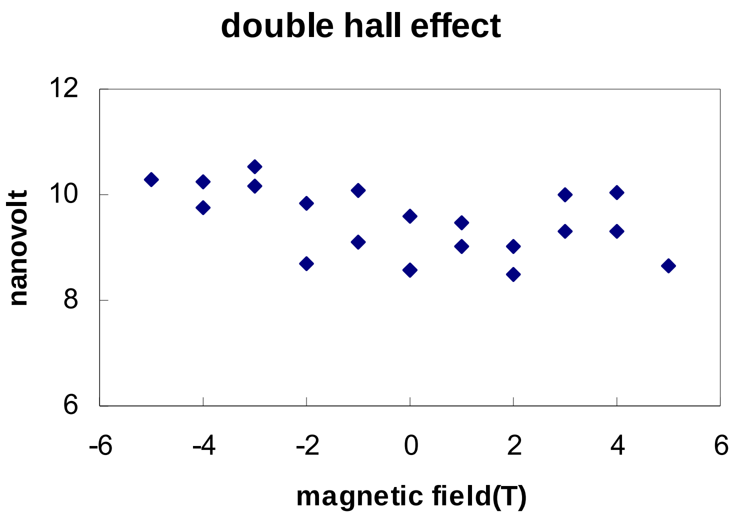

Figure 3.7 Double Hall Effect of the aluminum sample

Theories indicate that the voltage depended on B^2 due to the Double Hall Effect, where B is the external magnetic field. Figure 3.7 does not exhibit such dependence. The voltage at zero magnetic field is positive, which has the same sign as expected. However, single value measurement is not trustful. We are not able to rule out spurious effect that can be easily above 10 nanovolt.

We calculated the expected Spin Hall Effect and Double Hall Effect signal following Hirsch's theory. The resistivity in our experiment was much bigger than the resistivity used in Hirsch's calculation. In Hirsch's calculation, he used $2.7*10^{-11}\Omega\bullet$m as the electric resistivity for a single crystal aluminum bar, whereas in our measurement we measured $1.16*10^{-8}\Omega\bullet$m. Our resistivity value is comparable with values of thin film reported in literature [23, 44]. Double Hall Effect and Spin Hall Effect are inversely proportional to the resistivity of the material. The signal in our device is estimated in the order of 10^{-12} volt. Thermal noise between pads (~1kΩ internal resistance at 4.2K) is about 10^{-9} volt. The Spin Hall Effect and Double Hall Effect signal are much smaller that the thermal noise so that they are beyond the measurement capability. Tremendous amount of effort had been devoted to decrease electric resistivity of aluminum film. We tried annealing the thin film, evaporating with purer aluminum source and evaporating film with electron gun evaporation under ultra high vacuum (10^{-9}torr). None of these techniques have decreased the resistivity of aluminum thin film significantly. It is not wise to expect the resistivity in thin film as low as the resistivity in single crystal bar[45, 46]. Our resistivity is comparable, if not better, with thin film values in literatures[23, 44].

3.2.2 Experimental result in gold thin film

In Section 3.2.1, measurement results in aluminum samples are presented. We have not observed Spin Hall Effect and Double Hall Effect. One reason is that the resistivity of the thin aluminum film is much bigger than the resistivity in single crystal aluminum bar, which leads to a much smaller signal. The calculated signal in aluminum film is even smaller than the thermal noise.

At the time we finished the experiments describe in Section 3.2.1, Intrinsic Spin Hall Effect is proposed [16, 17] where spin-orbit interaction is believed to be crucial for the Spin Hall Effect. It is useful to measure Spin Hall Effect in strong spin-orbit systems where the Spin Hall Effect is expected larger. gold which has larger spin-orbit interaction than aluminum is the material we are going to study next.

We employed the same fabrication method as in Section 3.2.1, but evaporated germanium/gold instead of aluminum. Germanium layer improves adhesion between gold thin film and the silicon substrate. The thickness of the film is about 58Å of germanium (adhesion layer) and 210Å of gold. The sample was measured at 4.2 Kelvin. For convenience, we label the pads with numbers, Figure 3.8.

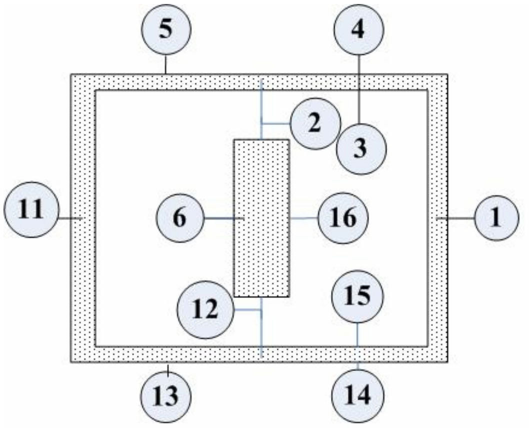

Figure 3.8 Simplification of pads coding

Positive magnetic field means the field is perpendicular and goes into the sample in this work. The measurement current is usually 10μA, which corresponds to a current density of $1.2*10^7$A/m^2 in each of the two identical current carrying strips.

Similarly, we measured the voltage between pads 5 and 4. The voltage was 196µV with a measurement current of 2µA. The current in each of the two identical strips was 1µA. The geometry of the current strip between pads 5 and 4 is 1390µm*20µm*210Å. The electrical resistivity is calculated as $5.9*10^{-8}$Ω•m. In [45] the bulk resistivity is $2.2*10^{-8}$ Ω•m. Our result is slightly larger than the bulk value. This is normal because the resistivity increases in thin film presumably due to surface scattering[45, 46].

For Ordinary Hall Effect, we measured the voltage between pads 14 and 4, pads 14 and 15, and pads 3 and 4 with magnetic field, Figure 3.9. In all of the measurement, linear dependence with magnetic field is observed. From the magnitude of the linear slope, the hall coefficient R_0 is calculated as $9.3*10^{-11}$ m^{3}amp^{-1}sec^{-1}, which is consistent with values in the literary [19]. The slope in Figure 3.9b) and Figure 3.9c) are almost the same, which indicates that the current density in each strip are almost same.

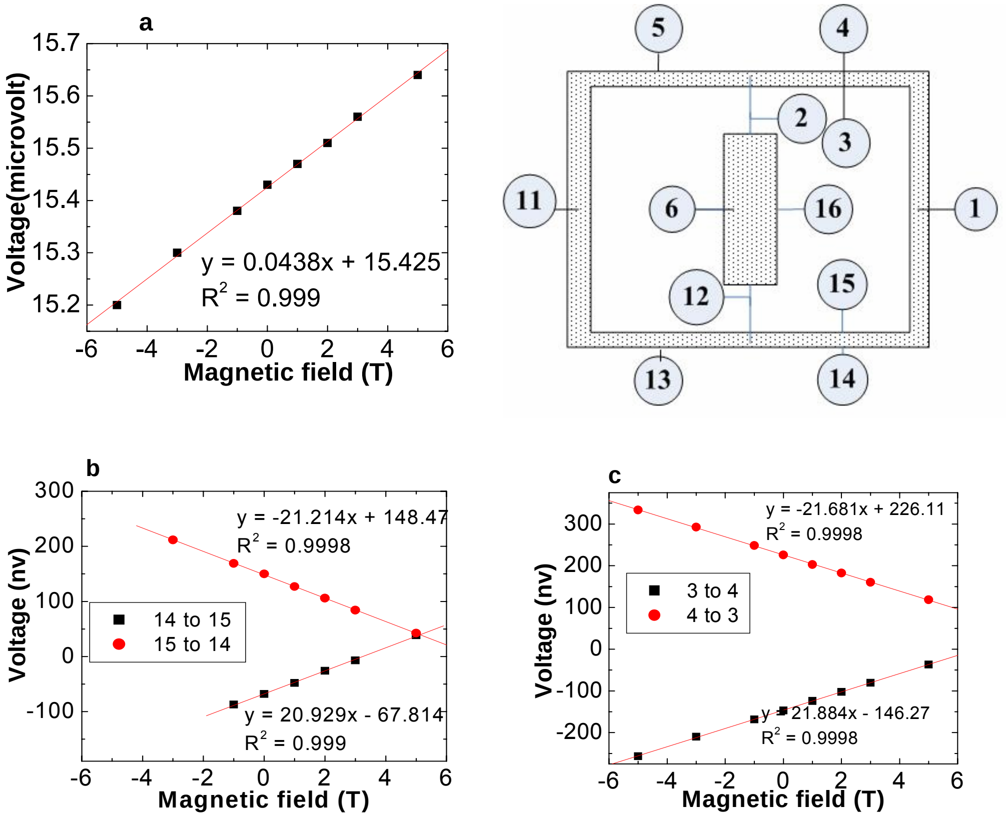

Figure 3.9 Normal Hall Effect Measurement of gold sample. Voltage measured a)between 14(V+) and 4(V-). b)between pads 14 and 15.c)between pads 3 and 4.10μA current was driven from pad 11 to 1.

In order to measure Double Hall Effect and Spin Hall Effect, we measured the voltage between pads 6 and 16 in magnetic field, Figure 3.10.

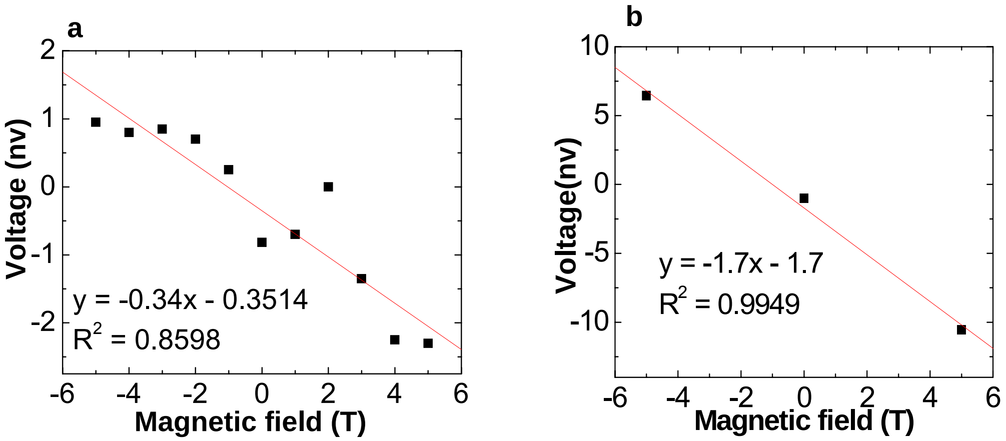

Figure 3.10 Double Hall Effect measurement of gold sample at different measurement current. a)10μA, b)50μA

At lower measurement current of 10μA, the voltage between 6 and 16 has no quadratic dependence with B as expected. The behavior in Figure 3.9a) is more like a linear dependence, not a quadratic dependence as we expected from Double Hall Effect. The measurement resolution is about 2nv. The variation of the data in Figure 3.10a) has similar size as the measurement resolution. The measurement current was increased to 50μA to increase the signal, Figure 3.9b). At larger current, the voltage between pads 6 and 16 linearly depends on the magnetic field, which is out of our expectation. It is experimentally confirmed that 50μA measurement current does not cause observable heating effect to our sample at 4.2K.

The origin of this linear dependence is studied. Ideally, no current is flown through the transverse strip if the two longitudinal strips carry the same amount of current by design. However, nothing is perfect. The two current paths fabricated by photolithography may differ slightly. If the linear dependence with magnetic field in Figure 3.10 is due to Ordinary Hall Effect, from the slope and the Hall resistivity R_0, the current responsible for such linear behavior in magnetic field is about $5.8*10^{-7}$A.

In Figure 3.9b) and Figure 3.9c), the slopes of the Normal Hall Effect have some difference (-21.214*nv/T* Vs -21.681*nv/T*). If assuming the two longitudinal strips have the same width at the position of the Hall crosses, the Hall voltage was proportional to current ($V_H/B=R_0*I/W$, where V_H is the Hall voltage measured, R_0 is the Hall coefficient, I is the current flowing through the strip, W is the width of the current strip). The current in the upper right strip is slightly bigger than the current in the lower right strip. The current difference must come from a small current flowing through the transverse strip. The current flowing through the transverse strip with respect to the total current is estimated from the magnitude of $(V_{3\text{-}4}-V_{14\text{-}15})/(V_{3\text{-}4}+V_{14\text{-}15})$~1%. This means that about 1% of total current flows through the transverse strip. From the slope of measurement in Figure 3.10b), the current in the transverse strip was estimated about $5.8*10^{-7}$A, which is about 1% of the total current 50μA. In this rough analysis, we assume that the width of two Hall crosses have the same width so that the slope difference in Figure 3.9b) and c) is purely due to different current magnetitude. Small difference in the width of the current carrying strips at the place of Hall Effect measurement may also lead to different slope in the Ordinary Hall Effect measurement in Figure 3.9b) and c). The width of the current strips was measured under SEM. The rough edge of the current strips patterned by photolithography prohibited precise measurement of the strip width. However if the slope difference of the Normal Hall Effect in Figure 3.9b) and c) is due to the width difference, 1% of the current strip width (20μm) corresponds to 200nm difference in width. This is very unlikely since our SEM system has 10 nm resolutions. The current difference is possibly due to some defects in the current paths which lead to different resistance in the circuit.

In micrometer size gold patterns, we have not observed the Double Hall Effect and Spin Hall Effect as expected. Both Spin Hall Effect and Double Hall Effect (in the same order) are proportional to $1/\rho$, where ρ is the resistivity of the gold film. As discussed in Section 3.2.1, the resistivity in thin films is much larger than the resistivity in single crystal bar [45, 46]. The larger resistivity in thin film leads to a much smaller Double Hall Effect and smaller Spin Hall Effect signal. Experimentally, the Spin Hall Effect is much smaller than the values 58nv predicted by Hirsch[14]. If using the resistivity obtained from experiments, the Spin Hall Effect decreased to 65pv (not 58nv) in the proposed device [14].

In Hirsch's estimation, he used R_0 for R_s. The anomalous Hall coefficient R_s can be estimated from [23]. In [23], the Spin Hall Effect without the diffusion contribution is:

$$V_{SH} = \frac{j_x Lt * P\sigma_{SH}}{t{\sigma_c}^2} = \frac{j_x LP\sigma_{SH}}{{\sigma_c}^2} \tag{3.8}$$

where V_{SH} is the Spin Hall voltage without spin diffusion, j_x is the current density, L is the width of a strip, P is the spin polarization rate of the current, σ_{SH} is the Spin Hall conductivity, and σ_c is the conductivity of the studied material. From Hirsch's theory, for a paramagnetic system with net magnetization, the Spin Hall voltage is:

$$V_{SH} = \mu_0 R_s MLj_x \tag{3.9}$$

where R_s is the anomalous Hall coefficient, M is the net magnetization in a paramagnetic system, L is the width of the system, and j_x is the current density. The net magnetization M can be written as:

$$M = (n_\uparrow - n_\downarrow)\mu_B = nP\mu_B \tag{3.10}$$

where $n_{\uparrow,}$ $(n_\downarrow)$ is the density of spin up (down) electrons, n is the total carriers' density. n is related to the Ordinary Hall coefficient in metals by:

$$R_0 = \frac{1}{ne} \tag{3.11}$$

Combining equation (3.8), (3.9), (3.10), (3.11), R_s is found as:

$$\frac{R_s}{R_0} = \frac{e\sigma_{SH}}{{\sigma_c}^2 \mu_0 \mu_B} \tag{3.12}$$

If using the value in [23], σ_{SH} is $2.7*10^3$ $(\Omega\mathrm{m})^{-1}$, and σ_c is $1.7*10^7(\Omega\mathrm{m})^{-1}$ for a 25nm thick aluminum film, the ratio of the Anomalous Hall coefficient to the Ordinary Hall coefficient is estimated as:

$$\frac{R_s}{R_0} = 0.12 \pm 0.027 \tag{3.13}$$

From equation (3.13), the Anomalous Hall coefficient is about 10 times smaller than the Ordinary Hall coefficient in aluminum thin films. This is possibly due to small spin-orbit interaction of aluminum.

The signal in our device is 10 times smaller than the signal proposed because of the geometry difference in design. The measurement resolution is 2nv, determined by averaging the same signal over four minutes for several times and choosing the maximum deviation as measurement resolution. The estimated Double Hall Effect and Spin Hall Effect signal is much smaller than our measurement resolution.

In this experiment, Double Hall Effect was the second order effect, which was driven by Ordinary Hall Effect. In our experiment, we did not observe a linear dependence with the external magnetic field between the two inner sides of the longitudinal current strips by measuring voltage between pads 3 and 15. Therefore, there is no voltage source to drive the Double Hall Effect in our system. The Spin Hall Effect which is Double Hall Effect at zero magnetic field could not be extracted from the measurement of Double Hall Effect.

Single point measurement of Spin Hall Effect at zero magnetic field is not conclusive. Although there is a reading across the transverse strip between pads 6 and

16, we could not root out the effect of misalignment. In Figure 3.10b), we measured -1.7nv y interception. The sample was checked under SEM. The width of the pads 6 and 16 is about 2 μm. Due to the poor edge definition by photolithography and corner rounding, we could not measure the misalignment precisely. The maximum possible misalignment of pair 6 and 16 was estimated to be 0.1μm. Using the parameters from the experiment (resistivity$5.9*10^{-8}\Omega\cdot m$, 1% of the measurement current flowing through central strip), 0.1μm misalignment can cause 5nv in voltage measurement when the measurement current is 50μA. The negative interception 1.7nv is possibly due to misalignment. At this point, we are only able to estimate that the upper limit of the Spin Hall Effect in this system must be smaller than 7nv (5nv due to possible misalignment and 2nv due to measurement resolution).

When we started Spin Hall Effect experiment in gold in early 2003, spin diffusion length of gold thin film was not available. Until later 2004, Y. Ji[32] measured the spin diffusion length in gold thin film of about 63±15nm. The transverse strip in our sample is 30μm by 100μm, which is much larger than the spin diffusion length of gold. This might be another reason that we did not measure the Spin Hall Effect in our system. It is possible to make isolated features smaller than the spin diffusion length of gold thin film. However, it is impossible to make similar patterns as studied in this chapter within the spin diffusion length of gold thin film.

3.3 Conclusion

To summarize our work in this chapter, we developed a methodology to study the Spin Hall Effect in aluminum and gold thin film. The methodology lifted up misalignment and interface resistance problems in the proposed experiment in [14]. The sample was measured at low temperature with 2*nv* measurement resolution. However, we did not observe the Double Hall Effect in gold and aluminum thin film. This is due to the higher resistivity of the thin film and the small anomalous Hall coefficient in aluminum which lead the Spin Hall Effect signal 5000 times smaller than the value in [14]. Single point measurement of Spin Hall Effect was not conclusive in this experiment. The upper limit of the Spin Hall Effect signal in our system was set to be 7nv.

The Spin Hall Effect experiments presented in this chapter is a second order effect. The Double Hall Effect is driven by an Ordinary Hall Effect. The Ordinary Hall Effect in metal thin film is in the order of nanovolt due to the high charge carriers' concentration. The Double Hall Effect and the Spin Hall Effect are in the order of picovolt. The size constraint of the spin diffusion length in paramagnetic thin film urges to study the Spin Hall Effect in nanometer size regime. In the next chapter, a more direct experimental method in nanometer size samples is presented.

CHAPTER IV

SPIN INJECTION EXPERIMENT

In Chapter III, the Spin Hall Effect was measured in micrometer size aluminum and gold thin film patterns. The signal was four orders of magnitude smaller than expected. The experiments are designed to extract Spin Hall Effect from the Double Hall Effect which is driven by the Ordinary Hall Effect. However, we have not observed the Double Hall Effect. Both Double Hall Effect and Spin Hall Effect are second-order effects, and are smaller than the thermal noise in the system.

The spin diffusion length in gold thin film is 63±15nm [32], which makes our devices in Chapter III not favorable. In this chapter, we will present sample fabrication process which will be used to produce a first-order Spin Hall Effect.

4.1 Key ideas of the experiments

In Spin Hall Effect, when an electric current flows in a paramagnetic system, spin-up electrons are more likely directed to the right (left) of the current flowing direction while spin-down electrons are more likely to the left (right). A pure spin current is generated perpendicular to the charge flowing direction and spin imbalance exists at the edges of the current path. To detect the Spin Hall Effect in paramagnetic systems is challenging. Due to equal number of spin-up and spin-down electrons in paramagnetic systems, there is no charge imbalance despite spin imbalance at the two edges of the current path. Commercially available magnetometers do not have enough resolution to detect the local magnetization caused by the imbalanced spins.

What happens if the current in the paramagnetic strip is spin-polarized? Because of Spin Hall Effect, spin-up and spin-down electrons are deflected to different sides of the current path due to the Spin Hall Effect. A charge imbalance is established at the two edges of the current strip as a direct result of unequal number of spin-up and spin-down electrons and the Spin Hall Effect. Moreover, the charge imbalance depends on the polarization direction. The charge imbalance, a direct result of Spin Hall Effect, can be measured with a simple voltmeter, ideally. The voltage built between the two edges changes sign when the direction of polarization is changed. So the key issue in this method is to generate spin-polarized current in paramagnet. A nature thought is to use ferromagnetic material. Ferromagnetic electrodes as spin injectors and spin detectors has been demonstrated [23, 28-33, 47] in various systems.

If a ferromagnetic material is in contact with a paramagnetic material, when a current flows from the ferromagnetic into the paramagnetic material, the current in the paramagnetic material is spin-polarized near the ferromagnetic material[23, 29-35, 48-50]. For this special experiment, several issues are considered: 1, the ferromagnetic material is better to have a magnetization perpendicular to the sample plane. 2, the ferromagnetic material has reasonable low contact resistance with the paramagnetic material. 3, the ferromagnetic material is macroscopically accessible. 4, the dimension of the essential parts of the device is in the regime of the Spin Diffusion Length of the studied paramagnetic material. These four considerations make sample fabrication difficult.

A method to generate such devices is presented in this chapter. It aims to fabricate a nanometer size ferromagnetic rod perpendicular to a paramagnetic thin film patterned by electron beam lithography (EBL). The ferromagnetic rod has certain height/diameter ratio in order to have an easy axis perpendicular to the sample plane. If the Ferromagnet is magnetized by applying an external magnetic field along the easy axis, it maintains its magnetization even after the external magnetic field is removed. This ferromagnetic rod serves as a spin injector that sends polarized current into the paramagnetic layer. In the paramagnetic layer, electrons with different spins are directed to different sides. By measuring the voltage across the two sides, we expect to measure the Spin Hall Effect directly. Ferromagnet has an ability of detect electron’s spin depends on its magnetization [15, 31-33]. The ferromagnetic rod in this experiment might also function as a spin detector.

4.2 Sample fabrication

The fabrication process consists of two steps of electron beam lithography, two or three steps of thin film deposition, one step of liftoff and one step of electroplating.

Gold is firstly studied in this experiment because gold has strong spin-orbit coupling. In 2004, Yi measured that the spin diffusion length of gold thin film is about $63\text{nm} \pm 15\,\text{nm}$ [32]. This dimension has to be considered in designing experiment.

4.2.1 The first layer pattern fabrication

Silicon wafer is used as the substrate. Silicon wafer is sliced into about 1cm by 1cm square. The wafer is cleaned in an acetone bath with ultrasonic agitation for about 15mins. The wafer is rinsed with acetone and isopropanol sequentially, and dried with nitrogen gas. The substrate is baked on a hot plate at 160 degree Celsius for about 10 minutes to remove solvent accumulated during the cleaning process. 3% PMMA is applied onto the clean silicon wafer. The substrate is spun rapidly at 4000rpm which gives a PMMA layer of about 110nm thick. The substrate with PMMA is baked at 160 degrees Celsius for 90 seconds. After the wafer is cooled down, it is loaded into an electron beam lithography chamber. Details of electron beam lithography operation are introduced in Chapter II, subsection 2.2.

Electron beam lithography is perfect for writing fine features. Yet it takes longer to write larger contact pads even with large beam current. Ideally larger contact pads are fabricated with Photolithography and using E-beam Lithography to write fine feather only. However, in order to avoid complexity of alignment and interface contact resistance, we wrote both larger contact pads and fine features with E-beam Lithography. The writing condition is different when writing larger and smaller feathers. The magnification of Scanning Electron Microscope (SEM) determines the writing field meaning the maximum dimension that the system could write a pattern in. The larger the magnification is, the smaller the writing field is. 3300 Magnification (3300X) and low beam current are used to write the smallest features. With 3300X, the writing field is about 25µm by 25µm. Low magnification (35X) is used to write relatively larger contact pads. It is necessary to write intermediate features which connect larger contact pads and the finest features. The parameters for each layer are listed in table 1. In the table, B.C means beam current, C-C means center-center distance of adjacent exposure, and L-L means line-line distance of exposure.

Table 1 Parameters of the first step electron beam lithography

layer	Mag	B.C.	C-C	L-L	dosage(nC/cm2)
1	3300	10pA	10nm	10nm	350
2	330	50pA	20nm	20nm	300
3	35	800pA	40nm	40nm	220

After the PMMA is exposed by high energy electron beam, the sample is developed in a developer solution (MIBK: ISOPROPONAL=1:3, volume ratio) for 60 seconds. PMMA that is exposed to the electron beam is removed, while unexposed PMMA stays. A PMMA pattern is created.

Evaporation and liftoff process are used to transfer the PMMA pattern to the silicon wafer. Germanium and gold are sequentially evaporated onto the PMMA pattern in a vacuum (~$5*10^{-6}$torr) environment. The thickness of the gold film is about 25nm and evaporation rate is about 0.1nm/second. The germanium film is about 5.8nm and evaporated at a 0.1nm/second. The gold/germanium film covers the whole PMMA pattern. Part of the gold/germanium film has PMMA underneath (not exposed by the electron beam in the patterning process), and part of the gold/germanium film makes direct contact with the silicon substrate. The sample is then immersed into an acetone bath. Acetone removes PMMA together with the germanium/gold film above. The germanium/gold in direct contact with silicon substrate stays. Using this liftoff process, the PMMA pattern is transferred to a Ge/Au pattern. See process flow diagram in Figure 4.1.

The gold pattern designed for the experiment is schematically shown in Figure 4.2. The thickness of the film is 5nm/25nm (germanium/gold). The pattern has a 100 nm wide strip, along X direction defined in Figure 4.2, with big contact pads at both ends. Two detection probes form a Hall cross with the central strip. The smallest width of the two detection probes is about 50nm. Above the pattern are alignment marks. Alignment marks 1 consist of two narrow lines along Y direction with width of 100nm. The lower end of the alignment mark is about 20µm to the central strip. The two alignment marks are 2µm apart. One is 1µm left to the perpendicular part of the detection probes, and the other one is 1µm right. Larger alignment mark 2 and 3 are created right above alignment marks 1 for later alignment purpose.

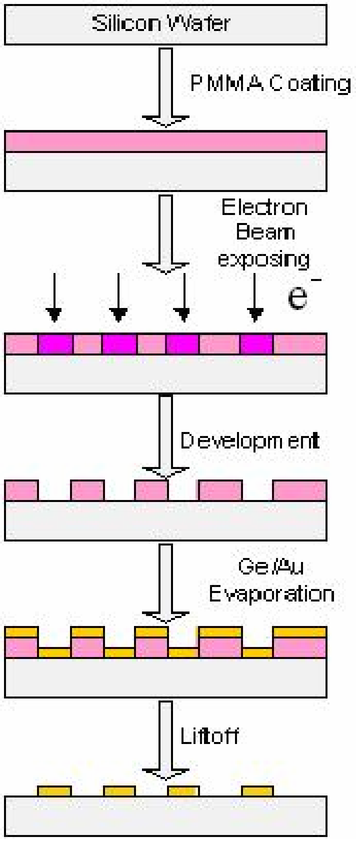

Figure 4.1 Process flowing diagram I of the first layer pattern fabrication

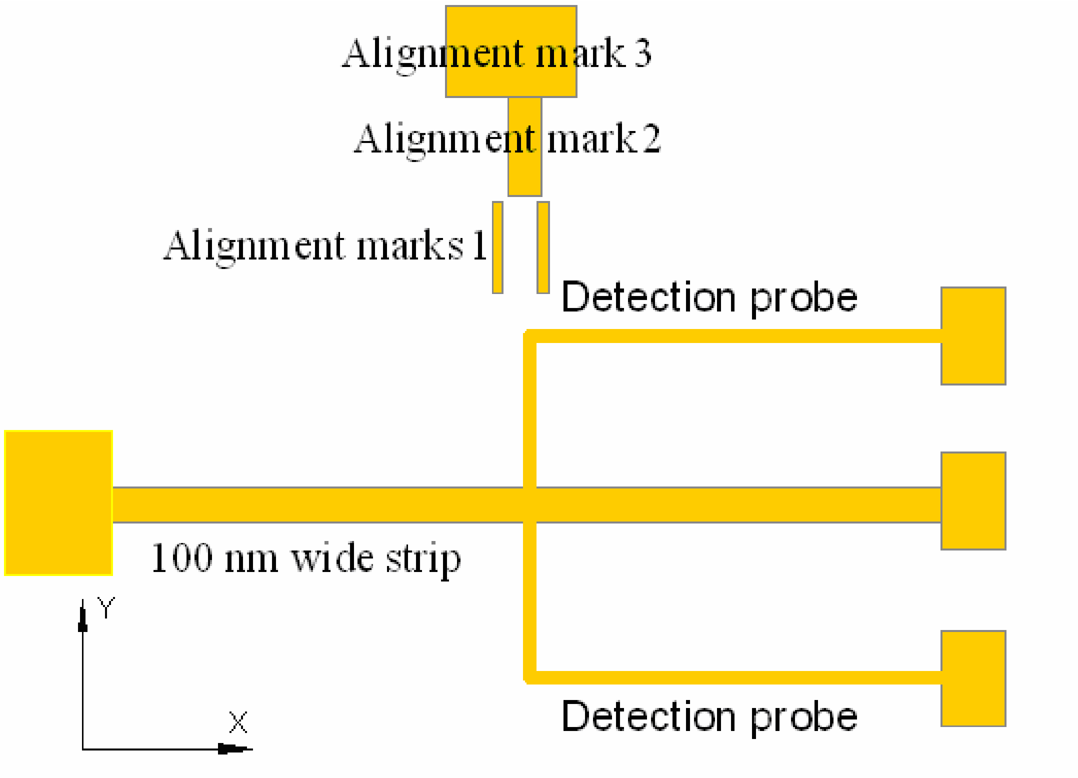

Figure 4.2 Top view of an EBL defined Ge/Au pattern. Central strip is 100nm wide.

4.2.2 The second step electron beam lithography patterning

The Ge/Au pattern fabricated in the previous step is cleaned with acetone and isopropanol and dried with nitrogen gas. 3% PMMA is spun onto the pattern at a spinning speed of 1500rpm. The spinning time is 60 seconds to ensure uniform coating. The PMMA layer is about 200nm thick. The PMMA layer is baked at 160 degrees Celsius for 90 seconds. After the sample is cooled, it is loaded into EBL chamber for the second step patterning.

The pattern written in this step is a series of dots (holes on PMMA after development) along the Y direction. This series of dots is positioned left to the perpendicular part of the detection probes as close as possible. There are two ways to write a series of dots. The first method is to write each dot like an individual pattern and then repeat the process to form a series. The second method is to write a single line while set the center-center distance to certain value so that the proximity effect is not enough to write a continuous line. One advantage for the second method is that it produces smaller dots. However, the biggest disadvantage is that this method of patterning depends too much on the condition of the EBL system. As the condition of the system changes, the size of the dots is slightly different. Reproducibility of samples written by the second method is worse than using the first patterning method. We prefer to sacrifice EBL resolution for reproducibility for this particular experiment. The flow diagram of the second step electron beam lithography is in Figure 4.3.

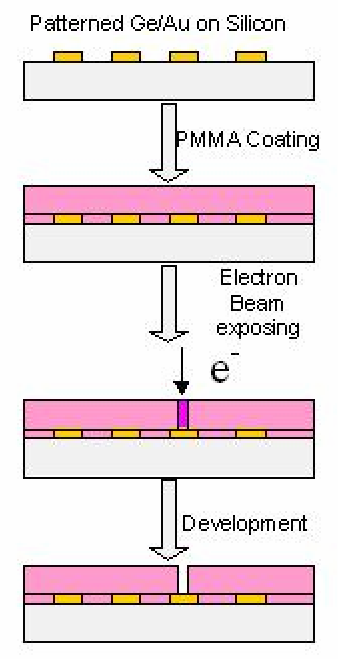

Figure 4.3 Process flow diagram of the second step EBL patterning

In the second step E-beam Lithography, alignment is crucial because the distance between the dots and the detection probes in Figure 4.2 should be within the Spin Diffusion Length of gold. The alignment marks prepared in Section 4.2.1 are used to determine the place to write the series of dots. The alignment marks are under a 200nm thick PMMA layer. It is difficult to locate the 100nm wide alignment marks 1 directly without exposing large area of PMMA. In order to solve this problem, two bigger alignment marks are written in the first step, Figure 4.2. Alignment mark 2 is 7µm wide. Alignment mark 3 is 45µm wide. All of the alignment marks are aligned along the Y direction so that they are found sequentially.

Alignment mark 3 is carefully located using a magnification of 200X. This magnification is chosen with reasons. Smaller magnification might not be sufficient to locate the 45µm wide alignment mark 3. Higher magnification gives smaller field of view which makes it more difficult to find features in a relative larger area. When locating the alignment mark 3, part of the PMMA layer is exposed to the electron beam. It is useful to start from the edge of the sample and look for the scratch created in the first step EBL. Once the biggest alignment mark 3 is located, the beam position is about 500µm away from the center of the first layer of pattern. The exposure area (field of view) has to be limited from now on. Larger magnification corresponds to smaller field of view. The maximum magnification to view the 45µm mark fully on the display screen is 2200X.

The relative positions of the marks are well known from the design in the first step pattern generation. The stage is carefully moved to the 7µm wide Alignment mark 2. The magnification used is 13000X to display the 7µm feature fully. Before locating the thinnest Alignment marks 1, a contamination spot is created to adjust the focus and stigmatism of the system. It is desired to optimize the condition of the electron beam lithography system as close to the final writing position as possible. After the system is optimized on the contamination spot, the stage is carefully moved to the finest (100nm) Alignment marks 1. The magnification used is 300,000X. For mechanic stage, it is very difficult to achieve alignment better than 1μm. For better alignment, a laser stage has to be used.

Fine alignment with a laser stage is complicated and prone to mistakes. There are two coordinate systems involved in the alignment. One is the coordinate system (X and Y) of the laser stage. The other one is the coordinate system of the Scanning Electron Microscope system (X' and Y'). These two coordinate systems are not necessarily well aligned. Movement in (X, Y) corresponds to physical movement of the sample. Movement in (X', Y') corresponds to the movement of the SEM image on the screen. Movement in (X, Y) does not necessarily correspond to the same movement in (X', Y'). If the same pattern is written at different locations by moving the stage, they may not align as desired. In Figure 4.4, three squares are designed to write in a row. Each pattern is written along (X', Y') coordinate system while the stage is moved in (X, Y). Misalignment occurs, top row in Figure 4.4.

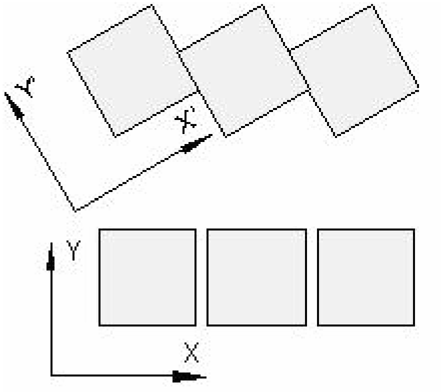

Figure 4.4 Schematic illustration of two coordinate systems. Bottom row, target patterns. Top row, misaligned patterns due to misalignment of (X,Y) and (X',Y').

One method to correct the misalignment is to rotate one of the coordinate systems. The laser stage can only move in the X and Y directions. It cannot be rotated. The SEM coordinate system can be electrically rotated by changing the scan rotation angle. This angle between the two coordinate systems is adjusted on a gold standard. After the SEM system is optimized, SEM image of gold granule is obtained. The stage is moved to certain distance in one direction and the movement of the SEM image is observed. The scan rotation angle is adjusted so that the image of the gold standard has the same direction of movement as the direction of stage movement. The scan rotation angle θ in our system is adjusted to 6.4° for our system. At this angle, movement in X or Y direction corresponds to the same movement in horizontal (X') or vertical (Y') direction on the SEM display screen. This angle is important for alignment, and should be checked frequently.

The pattern we are going to write in this step is parallel to the alignment marks. In EBL, patterns are written in (X', Y') coordinate system. The alignment marks need to be aligned along Y' direction. Once a sample is loaded into the electron beam lithography chamber, the sample, which is attached to the laser stage, cannot be physically rotated. The scan rotation angle is adjusted so that the SEM image of alignment mark appears perpendicular on the SEM display screen. The new rotation angle is labeled θ'. An ideal case is that θ' is equal to θ, so that the electron beam can be moved directly to the right position to start writing the pattern.

If the scan rotation angle θ’ is different from θ, special cares are needed to move the stage. The stage can not be simply moved by (0, d), where d is the distance in (X’, Y’) system between the beam position and the final position of patterning. Instead we move the stage by (-d*sin(θ’-θ), d*cos(θ’-θ)) (Figure 4.5). The distance d in our experiment is 18μm. Even though a small difference between θ’ and θ, d*sin(θ’-θ) might be significant. For 1° difference between θ’ and θ, d*sin(θ’-θ) is 0.31μm, which is significant compared to the alignment goal in this experiment (<200nm). There are two ways to move the stage. One is ‘go abs’ which means moving the stage to the absolute position (X, Y) no matter where the stage is. The second method is ‘go rel’ which means moving the stage with respect to the current stage location. Absolute coordinates is preferred over relative coordinates when moving the stage, because the inaccuracy of each relative movement adds up in relative stage movement. The accuracy of the laser stage movement is about 100nm in our system.

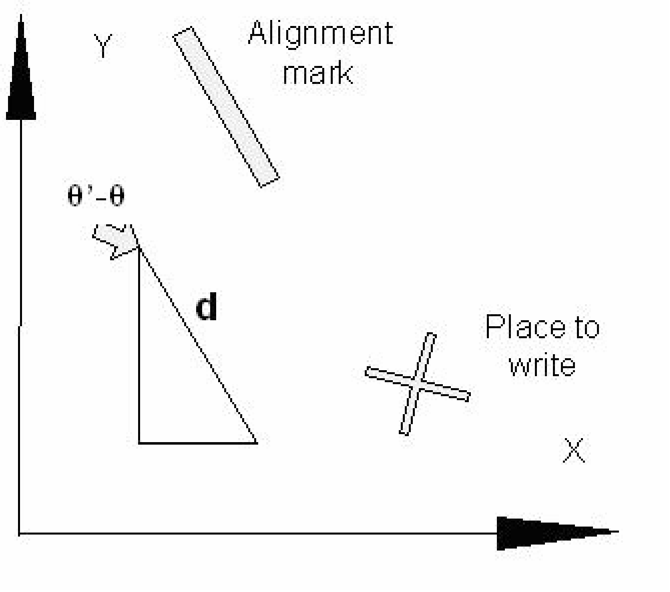

Figure 4.5 Illustration of stage movement for fine alignment

For a better alignment, the value of θ'-θ must be as accurate as possible. When the sample is loaded into the electron beam lithography chamber, one of the sample edges is aligned to one side of the laser stage, unfortunately only through eyes. In the first step of patterning, the scan rotation angle is adjusted until the wafer edge appears parallel to X' or Y'. In the second step of patterning, the scan rotation angle is adjusted to θ' so that the same edge appears parallel to X' or Y'. The sample edge is used to adjust the scan rotation angle roughly. Fine adjustment of the scan rotation angle is performed on the alignment marks where patterns are smaller and the edged of the alignment marks are better defined.

After the tedious steps of alignment, a series of dots is written. The overall length of this series dots is 25µm. The electron beam lithography system is optimized to write dots of about 50nm in diameter. The dosage used in this step for the dots is 250nc/cm^2. The distance between dots is set to 130nm so that only one, at most two, dots fall onto the central strip (Figure 4.6).

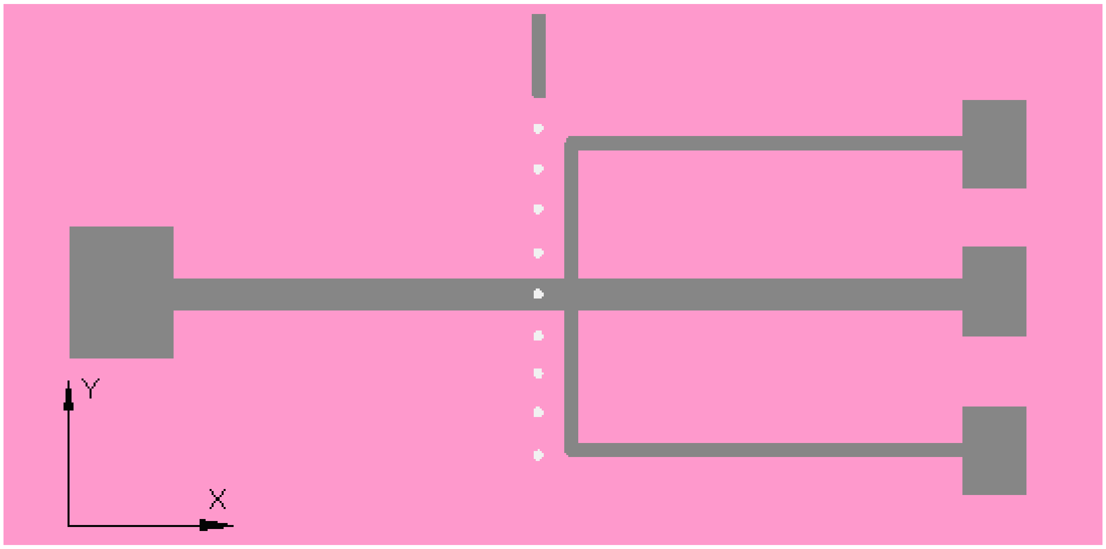

Figure 4.6 Schematic top view of the sample after the second step EBL and development

This second step of electron beam lithography is much harder than the first step EBL. Locating the alignment marks through a 200nm thick PMMA is very difficult. Accurate alignment described above is complicated and prone to mistakes. The dot diameter should be small in order to achieve a relatively high height/diameter ratio. A 50nm diameter dot in 200nm thick PMMA is probably close to the system's lowest capability.

4.2.3. Electroplating

Principle of Electroplating has been introduced in Chapter II. During electroplating process, metal ions in the plating solution are attracted to the cathode and form a metal layer on the cathode. In this experiment, nickel is electroplated on samples made in Section 4.2.2. The bottom Ge/Au pattern is connected as a cathode. The PMMA pattern is an electroplating mask which isolates the electroplating solution to the area where electroplating is not desired.

There are two methods to control the electroplating process. One method is to use a front electrode to monitor the voltage between the front electrode (a metal layer on top of the PMMA pattern) and the cathode (the Ge/Au pattern underneath the PMMA). The second method is to use an optical microscope to examine the grown material directly and determine when to stop the electroplating process.

In order to use a front electrode to control the electroplating process, the sample is loaded into a thermal evaporator after the PMMA pattern is written and developed in Section 4.2.4. After pumping down to 10^{-6}torr, a 15nm thick gold film is thermally evaporated through a shadow mask with ~1mm opening. The opening of the shadow mask is right on top of the series of dots patterned in Sec 4.2.2. This ~1mm wide gold strip is used as a front electrode to control the electroplating process.

Figure 4.7 shows a typical electroplating process of porous membranes [51-54].

V1/R measures the current through the electroplating circuit, which indicates the electroplating speed. V2 monitors the voltage between the front electrode and the back cathode. When the material fills in the pore and reaches the top electrode, V2 drops and the plating current V1/R increases[54].

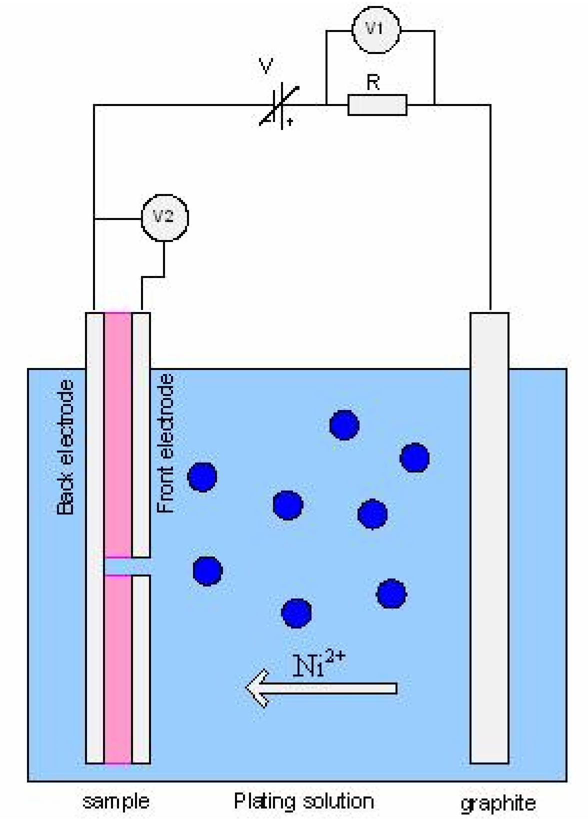

Figure 4.7 Schematic diagram of electroplating process

nickel is chosen as the ferromagnetic material because the crystal anisotropy of nickel is small compared to other ferromagnetic materials. In the electroplating process, the structure of the material is not controlled. Materials with smaller crystal anisotropy are favored because the easy axis is likely determined by the shape anisotropy[55]. Permalloy has zero crystal anisotropy. However plating alloy with controlled element percentage is not straightforward. Electroplating through PMMA patterns has been demonstrated [51-53, 56].

The macroscopic pads patterned in Section 4.2.1 are covered by PMMA. To make contact for the electroplating process, PMMA on one of the macroscopic contact pads in the bottom layer is carefully removed with acetone, and the exposed gold contact pad is connected as a cathode (back electrode). An extra piece of graphite or nickel plate, connected as an anode, is immersed in the nickel Sulfamate electroplating solution. A potential is applied between the cathode and the anode. The gold pattern in the solution is exposed to the plating solution through those holes patterned in Section 4.2.2. The remaining part of the gold sample is covered by PMMA, which prevents nickel growth. The nickel ions (positive charge) in the plating solution are attracted to the negative potential. nickel ions gain electrons from the cathode, and become nickel atoms. In Section 4.2.2, only one hole, at most two, falls onto the central 100nm wide strip, the only place that can supply electrons to nickel ions. Thus nickel can only grow in the one or two holes. Figure 4.8 is the schematic of the sample after electroplating. The plating current is usually several microamperes. Large current might destroy the sample.

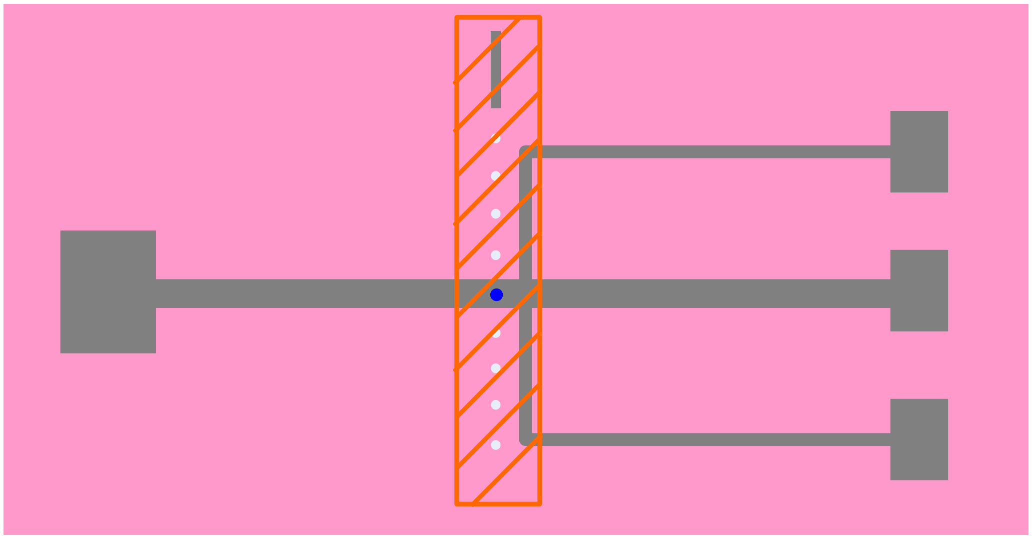

Figure 4.8 Schematic top view of a sample after electroplating with nickel rod grown.

After electroplating, ~1 mm wide gold strip is evaporated onto the top electrode. This gold layer protects the nickel rod from oxidation, and makes the nickel rod to top gold electrode contact stronger. The top electrode also provides macroscopic access to the nickel rod. Figure 4.9 described the process flow.

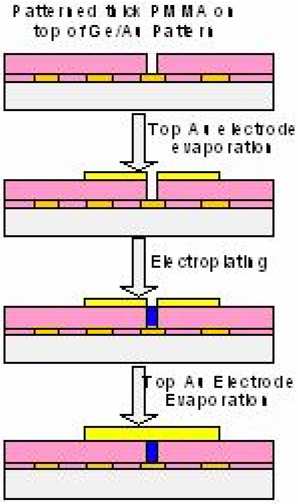

Figure 4.9 Top electrode fabrication and plating process

In our experience, using front electrode to control the electroplating process did not work very well. Sometimes V2 drops, but the contact resistance between the top electrode and the bottom electrode is very high (>10kΩ). From simple calculation and experience from successful electroplating, the resistance between the front and back electrodes is about 1KΩ. Sometimes no matter how long the sample is electroplated after V2 dropped, the contact resistance is still high. Sometimes we did not observe any V2 drop at all. Occasionally the top electrode was overgrown with nickel, but the resistance between the front and back electrodes was high. The yield of the fabrication process was very low. A more efficient method to control the electroplating method is needed.

The second method to control the electroplating process is to use an optical microscope to examine the electroplated material, in situ if possible. After the second step patterning in Section 4.2.2, the sample is treated similarly to the treatment in Section 4.3.1 except the evaporation of a top gold electrode. The sample is placed into the electroplating solution and starts electroplating. After certain time, usually from experience, the sample is taken out and inspected under a high resolution optical microscope if this step can not be done in situ. When the nickel slightly overgrows, the mushroom head of the nickel rod is observed under the optical microscope. A thick gold layer is deposited onto the sample through a shadow mask. The width of the strip is about 1mm. This gold strip serves as a contact electrode to the nickel rod and also prevents the nickel nanorod from oxidation.

In order to confirm that nickel is grown in the PMMA pore in this experiment, PMMA layer of a test sample prepared through the above steps was removed (sample is not usable anymore). This sample had 5 to 10 dots fell onto the central 100nm wide strip. The sample was loaded into a SEM chamber, and the sample surface was mounted perpendicular to the electron beam. Figure 4.10 shows a SEM image of the sample. Five dots (nickel) on the central strip are brighter than the rest dots (gold). The brightness difference is due to a height difference between the gold dots and the nickel dots. The nickel dots are bigger than the gold dots in size. This is because the gold dots were thermally evaporated, and the size of the each dot was determined by the top size of the holes patterned in Section 4.2.2. The nickel dots were electroplated. They filled the entire PMMA holes. In electron beam lithography process, high energy electrons is scattered in the PMMA. The bottom of the holes is bigger than the top of the holes. This undercut effect is normal for most lithographic process.

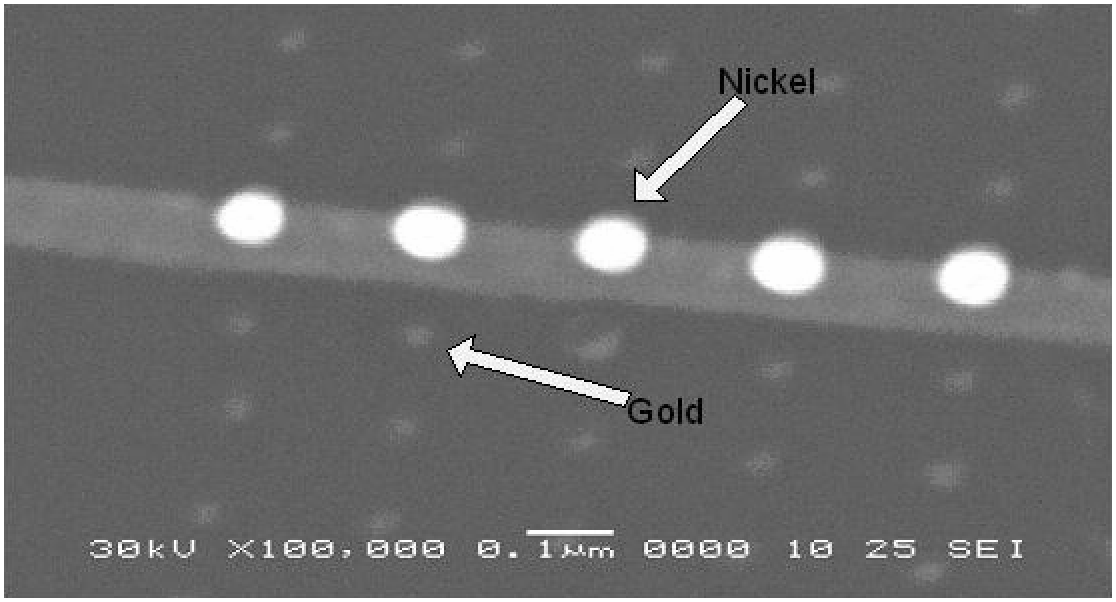

Figure 4.10 SEM image of a test sample after electroplating. The sample was mounted perpendicular to the electron beam.

Figure 4.10 does not show the overall shape of the nickel dot. To check the shape of the nickel dots, the SEM stage was tilted to 45°. Figure 4.11 is a SEM image of the same sample with a 45° tilted stage. The gold dots were thermally evaporated and about 20nm thick. The nickel dots have longer projection than the gold dots, which confirms that the nickel structure is perpendicular to the silicon wafer and the height is roughly about 200nm.

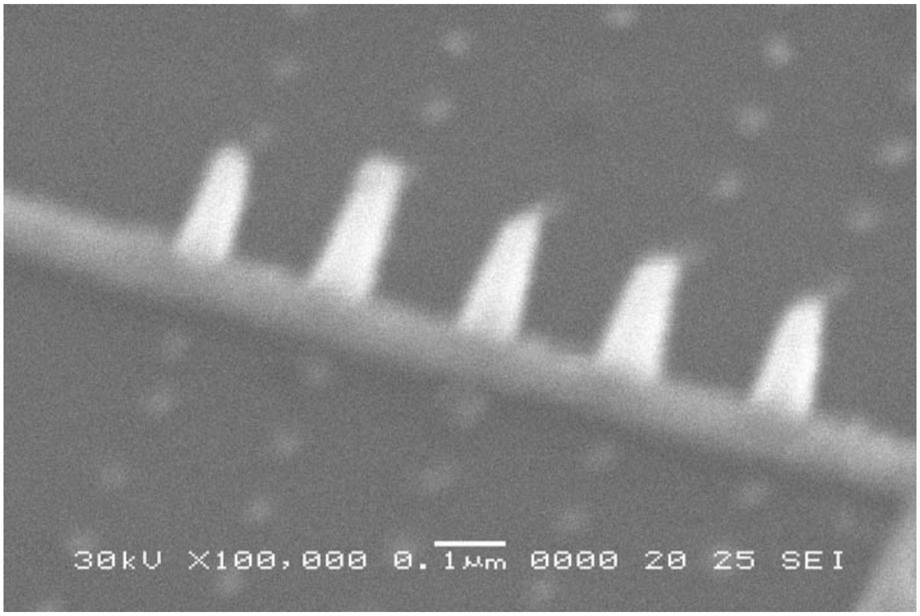

Figure 4.11 SEM images of a sample after electroplating with tilted stage. The image was taken while tilting the stage to 45°

The sample fabricated by the multi-steps process is a three layers system: top gold electrode/nickel rod/gold pattern, Figure 4.12. Only the nickel rod electrically connects the top gold strip and the bottom current pattern. The PMMA layer, not shown in Figure 4.12 to avoid confusion, physically supports the top gold electrode. The thickness of the PMMA should be bigger than certain value to avoid pinhole in the PMMA layer. Thick PMMA layer gives high height/diameter ratio for the nickel rod, but makes fabrication process difficult.

Although difficult to fabricate, some samples are ready for measurement, which will be presented in Chapter V.

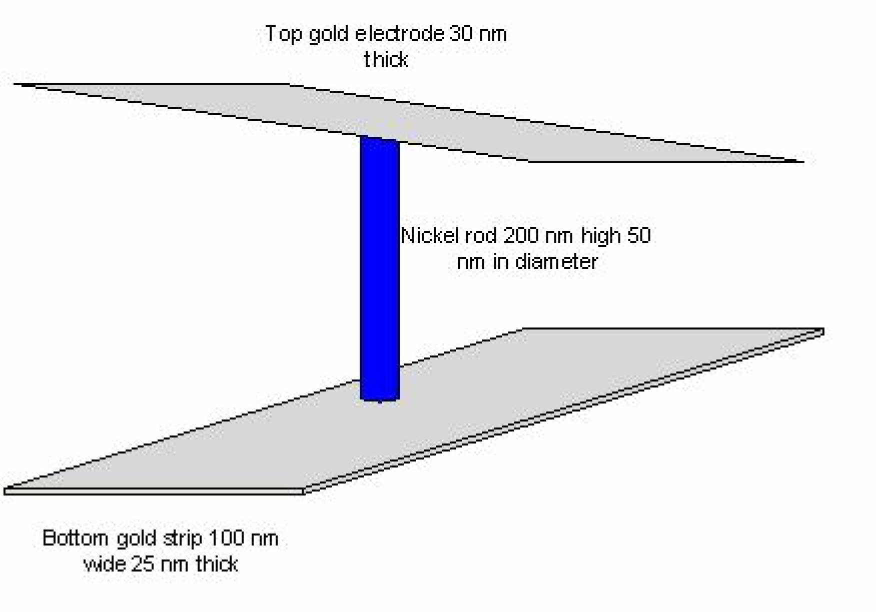

Figure 4.12 Schematic drawing of a tri-layer sample with ferromagnetic nanorod. Top gold electrode is supported by PMMA, not shown to avoid confusion.

CHAPTER V

MEASUREMENT AND DISCUSSION

In Chapter IV, the first layer gold pattern is fabricated by electron beam lithography patterning, metallization and liftoff process. The sample is coated with thicker PMMA (~200nm), and the second step electron beam lithography creates a series of dots. nickel is grown out of the PMMA hole that is right on top of the central 100nm wide strip. A gold layer with a width about 1mm is sputtered onto the nickel rod through a shadow mask. This multi-step fabrication process generates a tri-layer system: gold strip/nickel rod/gold pattern. For our convenience, the sputtered gold strip that is on the top of the PMMA layer is called the top gold strip. The gold pattern that is made in the first step electron beam lithography is called the bottom gold pattern. The top gold strip is separated from the bottom gold pattern by a 200nm thick PMMA layer. PMMA is insulating so that only the nickel rod electrically connects the top gold strip and the bottom gold pattern. This nickel rod has a height/diameter ratio of about 4 (200nm/50nm).

A top view of a sample is schematically shown in Figure 5.1. The contact pads are labeled with numbers. Pads 2, 4, 5, 6 are the macroscopic pads prepared in the first step electron beam lithography patterning. These four contact pads are underneath the

200nm thick PMMA. To make contact to these four pads, the PMMA that covers them is removed with a Q-tip wet with acetone. The rest PMMA which supports the top gold strip cannot be removed. The contacts 1 and 3 are the two ends of the top gold strip, which is on top of the PMMA.

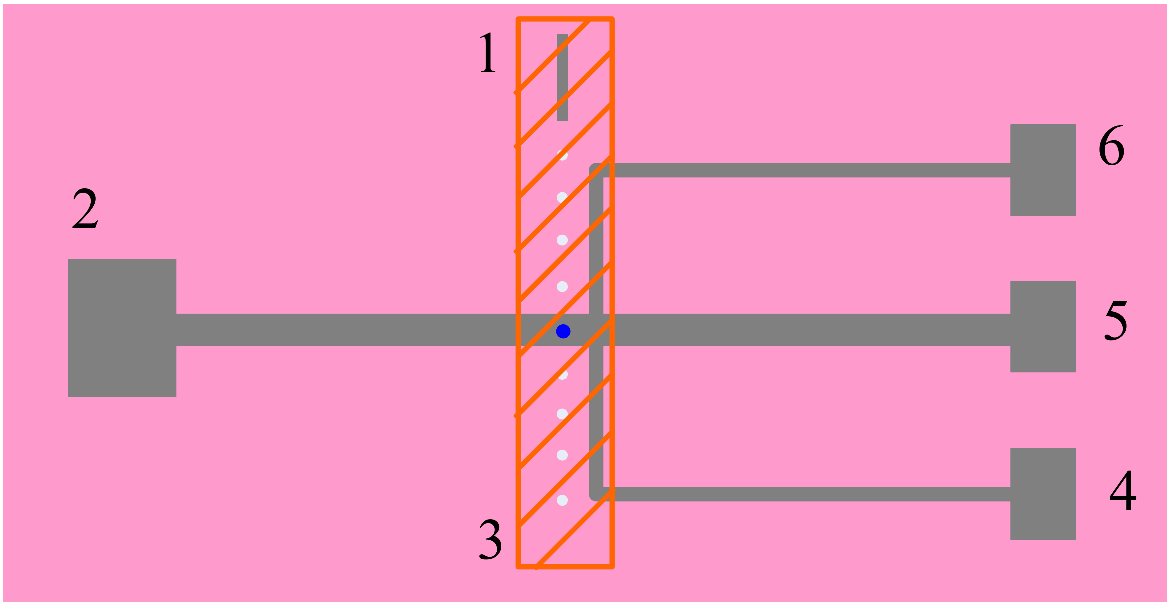

Figure 5.1 Top view of a sample after the fabrication process in Chapter IV

A control experiment was performed to make sure no significant current leaks through the PMMA layer. In the control experiment, the first gold layer was patterned as in Section 4.2.1. Then the sample was coated with 200nm thick PMMA (spinning speed 1500rpm). A top gold strip was sputtered directly on top of the PMMA. The resistance between the top electrode and the bottom gold pattern was over 1MΩ at room temperature. 200nm PMMA is pinhole free in this experiment.

After samples are fabricated successfully in chapter IV, the resistance between the two gold layers is measured. If the nickel rod electrically connects the two layers very well, a low resistance is measured. If the resistance is large (>10KΩ) between pads 1 and 2, that means the sample is bad. Extra care is needed when measure samples with nanometer size features. The nickel rod of nanometer size is so small that the measurement current from measurement devices may be large enough to destroy samples. A lock-in amplifier with a measurement current of 0.1μA is used to measure the resistance between various pads. Typical resistance between any two contact pads for gold samples is about 1KΩ.

Another important issue is electrostatic discharging. When the instrument connects to a sample, electrostatic discharging might destroy the sample. One method to solve this issue is to ground the sample before connecting each contact to the measurement system. The sequence of ground is important. It is not wise to ground each contact pad individually. The reason is that if there is any charge accumulation in the sample, when grounding individual pad, the charge flows through the sample. This current might be large enough to destroy the sample. The proper way to grounding consists of two steps. First, connect all contact pads together to make sure all contact pads are at equal potential. Then connect the sample to the ground. A switch box was built to protect the sample from electrostatic discharging. It consists of many two way switches. The upper pins of switches are connected together. Each contact pad is connected to the lower pin of a switch. When the switches are on, all of the contact pads are connected together. An extra switch controls the connection of upper pins of the switches to the ground, Figure 5.2.

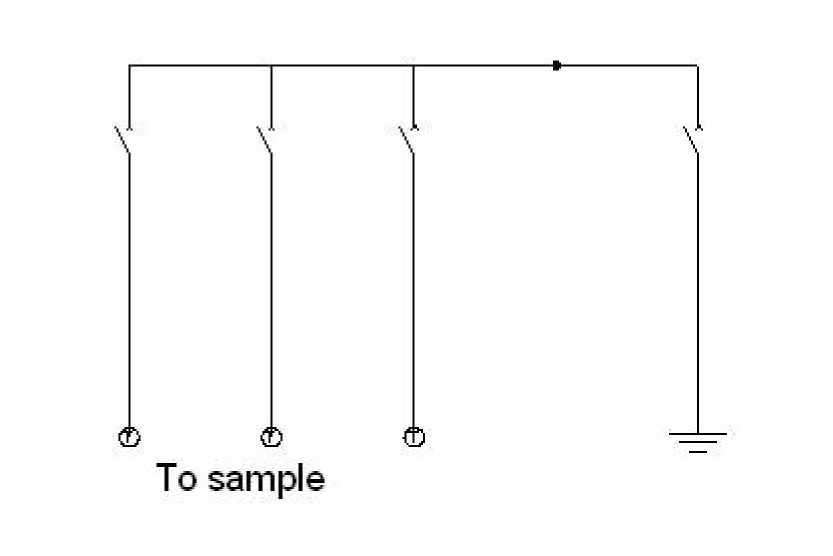

Figure 5.2 Schematic of sample grounding to prevent electrostatic discharging

In this experiment, gold and copper were used as the paramagnetic materials of the bottom layer. The measurement results are presented separately in this chapter.

5.1 Measurement of a gold sample

Gold was first studied in this injection experiment. Samples were fabricated by the multi step process described in Chapter IV. The thickness of the bottom layer Ge/Au is 5/25nm. In this section, measurement result of a sample labeled S061807 is presented.

5.1.1 Resistance of the nickel rod

The resistance of the nickel rod was measured with a typical four-wire AC measurement. The oscillation output of the lock-in amplifier (PAR 124) was 0.1v at 23Hz. A resistor of 1MΩ was connected in series with the sample to limit the measurement current to 0.1μA. The measurement current flew from pad 1 to 2. The voltage between pad 3 and 5 was fed into a preamplifier (PAR 113). The output of the preamplifier was fed into the lock-in amplifier channel A. The sample was cooled down to liquid helium temperature (4.2K). The resistance of the nickel rod was measured with a magnetic filed perpendicular to the sample, Figure 5.3. To increase the measurement resolution, the output of the lock in amplifier was fed into an Hp multimeter and the reading of the Hp multimeter was acquired by a computer through a GPIB interface. Each point in Figure 5.2 is the average of the raw data for four minutes. The peak-peak noise of the raw data is 20nv at 4K. A test signal was measured and averaged for several times. The data variation of each measurement was less than 2nv. We can conclude that averaging the raw data for four minutes increases the measurement resolution by an order of magnitude. All data in this chapter was acquired in this way unless specified. The magnetic field is perpendicular to the sample plane. Positive magnetic field means the field goes into the sample plane.

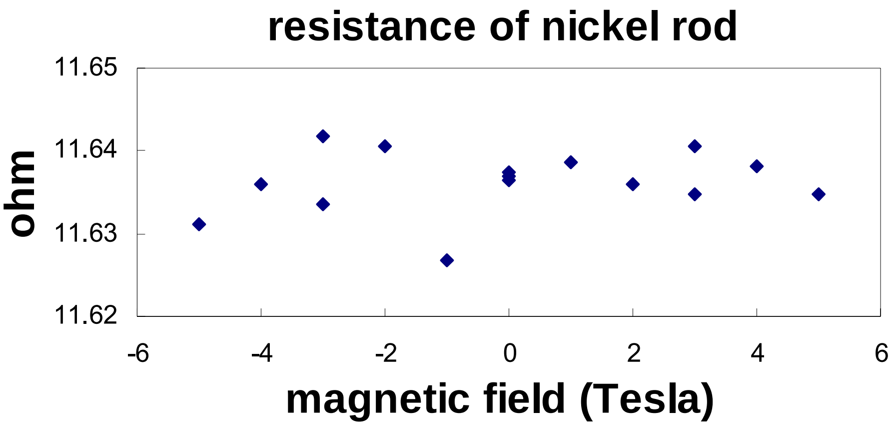

Figure 5.3 The resistance of the nickel rod in the magnetic field

In Figure 5.3, the resistance of the nickel rod does not depend on the magnetic field. The fluctuation in the data is about 0.02Ω. The measurement current is 0.1μA. This means that the voltage variation is 0.02 Ω*0.1μA=2nv, which is about the level of measurement resolution. The resistance of the nickel rod is 11.6Ω. If the length is 200nm, and diameter is 50nm, the resistivity of nickel is $1.13*10^{-7}$Ω•m, which is comparable with $17.6*10^{-7}$Ω•m in [57]. The bulk value of nickel is 8.1~11.5 μΩ•cm at room temperature.

5.1.2 Normal Hall Effect measurement

The two voltage probes of the sample enable an Ordinary Hall Effect measurement. The current flew from pad 2 to pad 5. The voltage between pad 4(V+) and 6(V-) was amplified with a PAR 113 preamplifier before fed into the lock-in amplifier. The measurement current is 5μA. The Ordinary Hall Effect data is in Figure 5.4. From the slope, the hall coefficient is calculated $7.3*10^{-11}$ $m^3amp^{-1}sec^{-1}$, which is close to the measurement results in Chapter III.

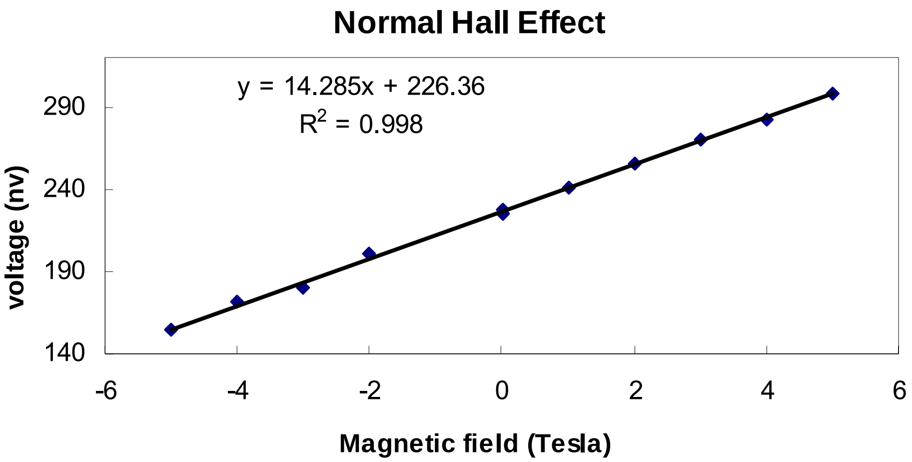

Figure 5.4 Ordinary Hall Effect measurement of a tri-layer sample

5.1.3 Spin injection experiment

The main purpose of this experiment is to inject spin polarize current into the bottom gold pattern. The nickel rod was magnetized by applying magnetic field and then removing the field. A current flew from the top gold strip to the right side of the bottom gold pattern through the nickel rod. The voltage between pad 4 and 6 was measured. Figure 5.5 shows the measurement scheme. A current flew from pad 1 to 5, and voltage between pad 4 (V+) and pad 6 (V-) was measured.

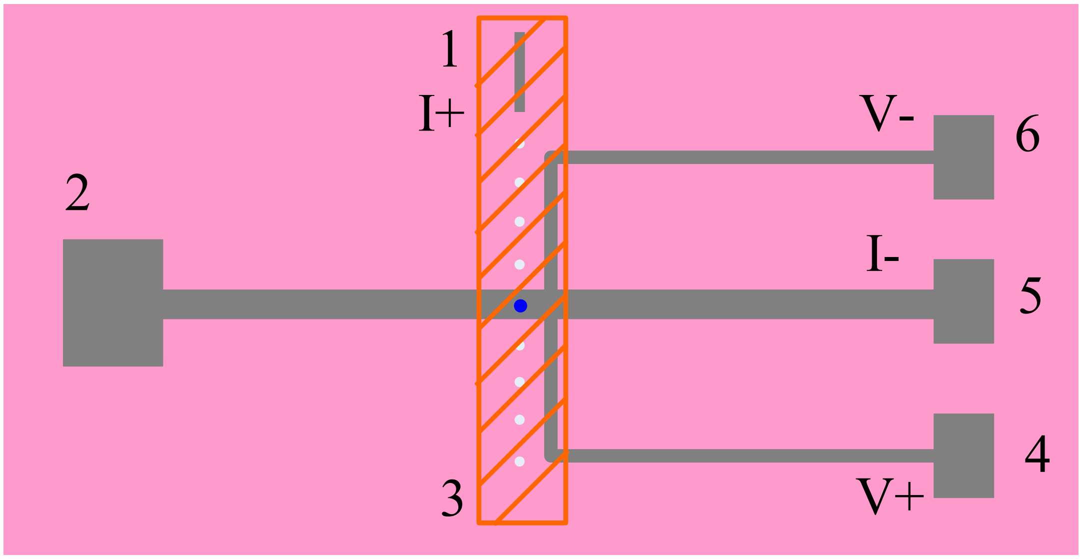

Figure 5.5 Measurement scheme of spin injection experiment

To magnetize the nickel rod, five Tesla magnetic field was applied perpendicular to the sample plane, and then removed the magnetic field. It is very likely that the nickel rod has an easy axis perpendicular to the sample plane due to its shape anisotropy. Because of the small size of the nickel rod, the magnetic properties are difficult to obtain directly. The easy axis of the nickel rod can not be experimentally confirmed. Spin Hall Effect, if successfully measured, will register different remnant magnetizations from different magnetic field preparations. M+ (M-)

is defined as the remnant magnetization of the nickel rod after the nickel rod is magnetized with a positive (negative) magnetic field. The current flew from pad 1 to 5. The voltage between pad 4 and 6 was measured with different remnant magnetizations (Table 2). Each point is the average of the raw data for four minutes. The measurement current is 5μA.

Table 2 The Voltage in different magnetization directions of the nickel rod

magnetization	M-	M+	M+	M-	M-	M+	M+
voltage(nv)	226.8	225.5	227.0	227.5	226.4	226.6	226.2

From Table 2, the voltage difference between different magnetizations is less than 2nv. It was discovered that the distance *L* between the nickel rod and the two voltages probe was quite long. Sample S061807 was fabricated before the electron beam lithography system was upgraded from a mechanic stage to a laser stage. The accuracy of alignment with mechanic stage is about 1μm. The sample S061807 was imaged under Scanning Electron Microscope to determine *L*. The PMMA on the sample was removed by soaking the sample in acetone bath for about 10 minutes. Then the sample was rinsed with acetone and isopropanol in sequence. The sample was dried and loaded into a SEM chamber. The image of the sample is shown in Figure 5.6. From the image, the closest nickel rod is about 2μm away from the two voltage probes. The spin diffusion length in gold is about 65nm. This might be the reason that we did not observe the Spin Hall Effect in this sample.

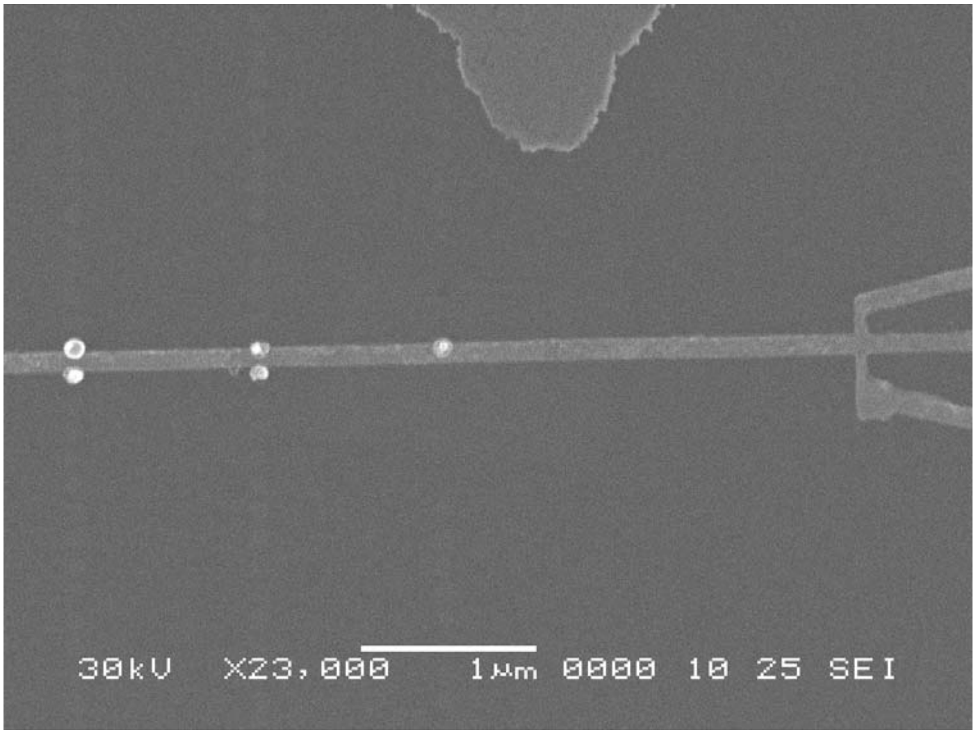

Figure 5.6 Scanning Electron Microscope image of the measured sample.

In order to detect Spin Hall Effect, it is necessary to fabricate the nickel rod closer to the two detection probes. A laser stage with 100nm movement accuracy is installed in summer 2007.

5.1.4 Measurement of a gold sample with fine alignment

The sample measured in Section 5.1.3 was aligned with a mechanic stage, where alignment was not well controlled. The sample had five nickel rods purposely to increase the yield of sample fabrication. The shortest distance between the nickel rod and the two voltage probes is about 2 μm. The spin diffusion length in gold film is about 65nm. The mechanic stage is not accurate enough to make alignment close to 100nm. A laser stage was installed in 2007.

Using a laser stage, better alignment has been achieved with the alignment method introduced in chapter IV. Several samples had been fabricated and measured. In this section, the measurement results of one sample labeled S090607 is presented. Other sample showed similar results. The thickness of the bottom gold pattern is about 25nm with 5nm germanium adhesion layer underneath. The distance between the nickel rod and the two voltage probes is about 400nm.

Ordinary Hall Effect was measured, as in Figure 5.7. From the slope, the Hall coefficient is calculated as $6.9*10^{-11}$ $m^3amp^{-1}sec^{-1}$.

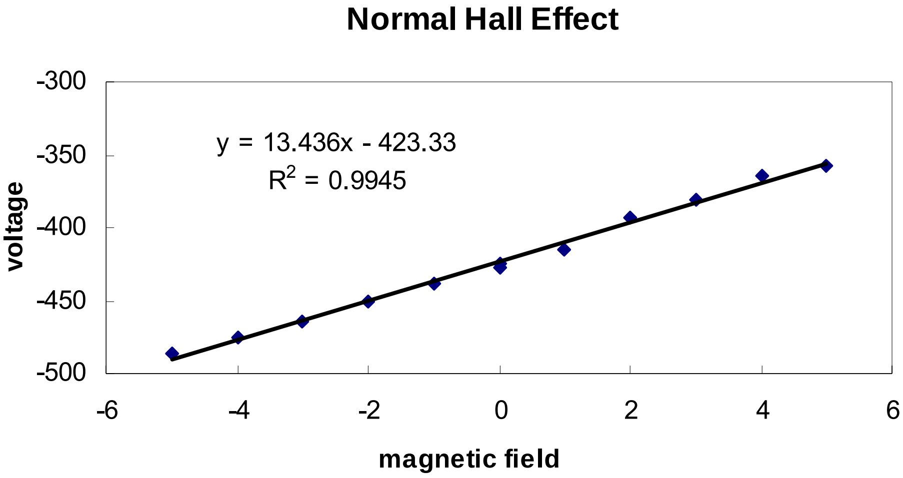

Figure 5.7 Normal Hall Effect measurement of sample S090607.

Spin injection experiment was performed in a similar way as described in Section 5.1.3. Current flew from pad 1 to 5. Voltage between pad 4 and 6 was measured. The voltage was measured in different magnetization directions. M=0 means the nickel rod has not been magnetized before. M-(M+) means applying a negative (positive) magnetic field perpendicular to the sample plane and then removing the field. Positive (negative) magnetic field means the field pointing into (out) the sample plane. The result is presented in Table 3.

Table 3 The Voltage in different magnetization directions of the nickel rod

M	0	M-	M+	M-	M+
V(nv)	-441.3	-441.1	-442.0	-442.8	-442.6

From the data in table 3, no significant voltage difference at different magnetization directions are observed as one expects from the Spin Hall Effect. After check the sample under SEM, the distance between the nickel rod and the voltage probes is about 400nm, still bigger than the spin diffusion length of gold (~65nm). Alignment in this multi-step process is difficult.

The best alignment achieved so far is about 100nm, Figure 5.8. Unfortunately, this sample is not usable after the fabrication process. The resistance between the top gold strip and the bottom gold pattern is 37KΩ. Typical resistance between the two gold layers including the resistance of two gold layers is about 1KΩ. The higher resistance in this sample may due to short electroplating time so that the top gold strip could not contact the nickel rod if the nickel rod did not fill out the PMMA pore completely.

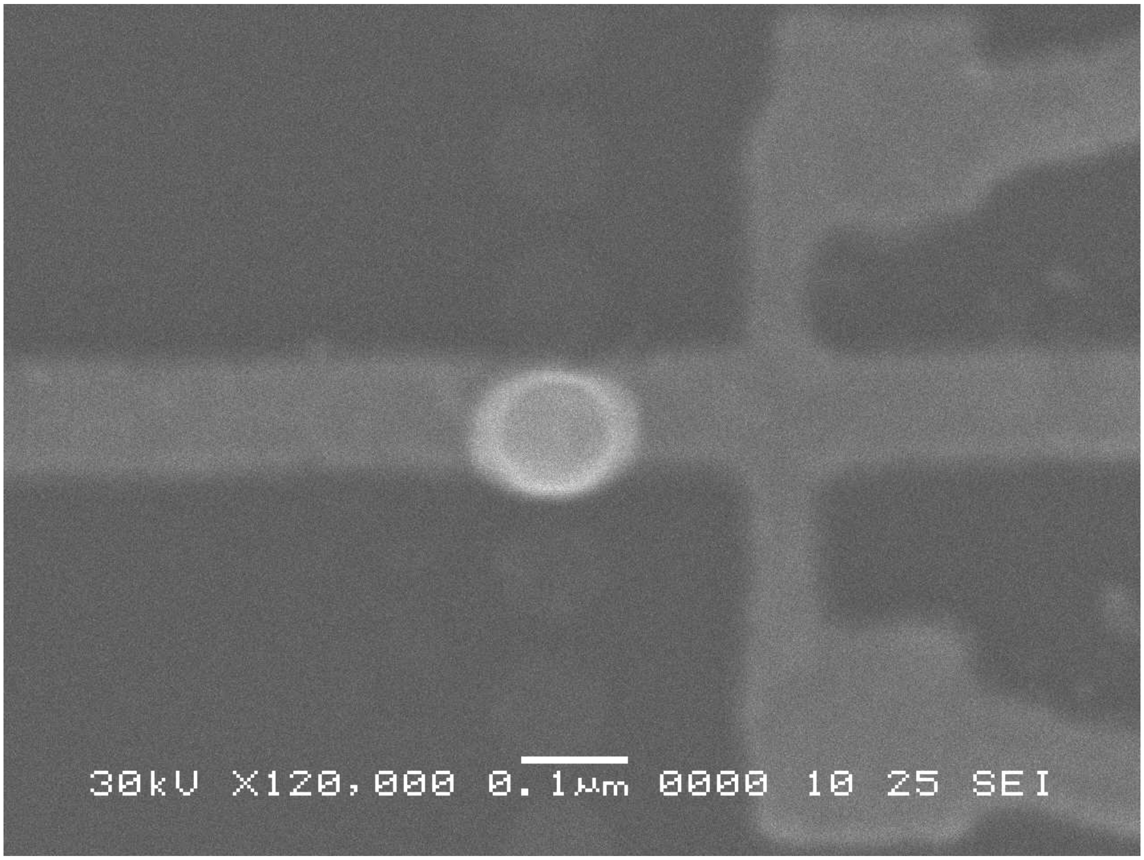

Figure 5.8 SEM image of a good alignment using a laser stage. The distance between the nickel rod and the two voltage probes was about 100nm)

The best alignment (100nm) achieved so far is still bigger than the spin diffusion length of gold thin film. To fabricate a sample with *L* less than 65nm is very difficult, where *L* is the distance between the nickel rod and the two voltage detection probes. The laser stage has a position movement accuracy of about 100nm. The scan rotation angle θ’ is hard to determine precisely. The alignment mark is underneath the 200nm thick PMMA. The SEM image of the alignment marks is blurring which make the scan rotation angle hard to adjust. 1° error in the scan rotation angel θ' corresponds to ~300nm misalignment in the horizontal direction (-d*sin(θ'-θ), alignment in Chapter IV). The distance between the alignment marks 1 and the final place to start writing pattern is 18μm. This distance d can not be shorter. Otherwise, the PMMA to be patterned is exposed during the alignment process due to proximity effect. It is possible to make more samples and hope one sample with the best alignment. However it is time consuming and may not worth the effort. The sample fabrication involves many steps. The yield is too low. It is useful to switch to systems with longer spin diffusion length, which made sample fabrication less stressful. Copper is a good candidate.

5.2 Measurement with a copper sample

In Section 5.1, measurement in gold thin film is presented. The spin diffusion length of gold was reported as 65nm, which made sample fabrication extremely difficult. Alignment to 65nm accuracy or better in a complicated sample fabrication process is challenging. It is useful to use materials with longer spin diffusion length. Jedema [33] reported the spin diffusion length of copper is about 1μm at 4.2k, and about 350nm at room temperature. Kimura reported that the spin diffusion length in a slightly thicker copper film was 500nm at room temperature [36].

The same fabrication method is used to fabricate samples with three layers: top gold electrode/nickel rod/ bottom copper pattern. After the first layer E-beam Lithography, Ge/Cu rather than Ge/Au in Section 5.1 was thermally evaporated. The thickness of the copper layer is 25nm. The thickness of the germanium adhesion layer is about 5nm. The measurement result is presented below.

The resistivity of the copper film at 4.2k was measured to be $1.7*10^{-7}\Omega\bullet m$, in reasonable agreement with the resistivity of 50nm thicker copper film reported as $3*10^{-8}\Omega\bullet m$[33]. The Ordinary Hall Effect measurement of the sample S012708 was presented in Figure 5.9. The measurement current is 5μA.

From the slope of Figure 5.9, the Hall coefficient is calculated as $5*10^{-11}$ $m^3amp^{-1}sec^{-1}$. There are 3.7μv offset in the Ordinary Hall Effect measurement. This offset is possible due to the misalignment of the voltage probes. Using the resistivity of copper film, the misalignment of the two voltage probes is estimated to be about 10nm.

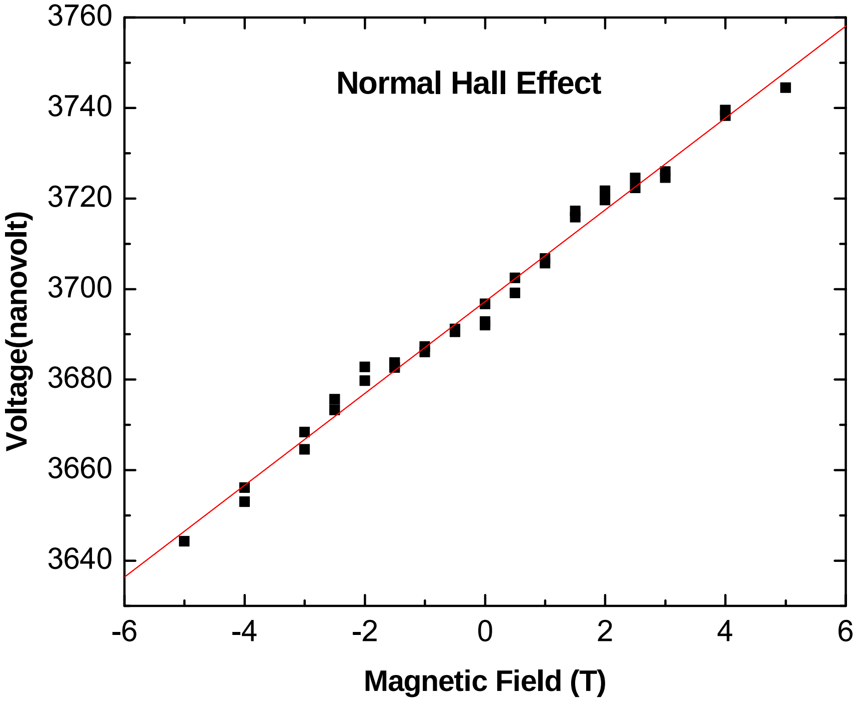

Figure 5.9 The Ordinary Hall Effect of a copper sample

To measure the Spin Hall Effect, a current was sent from the top gold electrode to the left side of the bottom copper pattern through the nickel rod, and the voltage between pad 4 and 6 was measured, Figure 5.10.

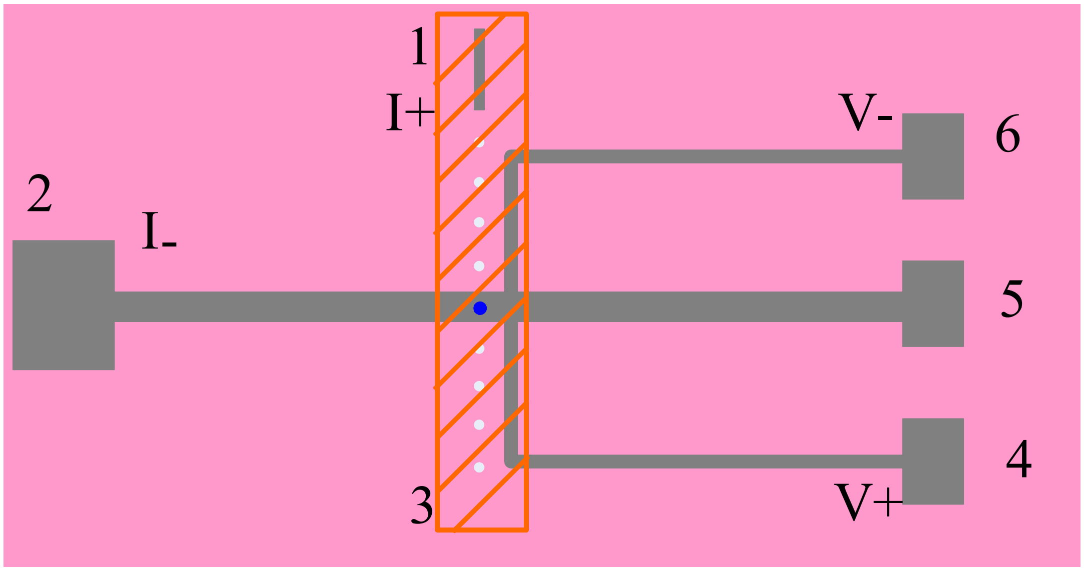

Figure 5.10 The measurement scheme of the spin injection experiment.

The current from the top gold electrode through the nickel rod into the bottom copper layer is spin polarized if the nickel rod is magnetized. The polarized electrons diffuse to the right side of the sample. As a result of Spin Hall Effect, we expect a voltage V_{SH} between pads 4 and 6 depending on the magnetization directions of the nickel rod. Unfortunately we did not see V_{SH} depends on the magnetization directions in this sample, Table 4.

Table 4 VSH measurement at different nickel rod magnetic field preparation

M	0	M-	M+	M-	M+	M-	M+	M-	M+
nv	-139.5	-139	-140	-140	-141.2	-141.3	-141.5	-142	-140.6

Ideally if the nickel rod is not magnetized, the voltage between pads 4 and 6 is zero because no electric current flow in the right side arm of the central strip. In Table 4, V_{SH} has an offset of about 140nv in this measurement at 4.2K. Even at room temperature, we observed over 100nv between pad 4 and 6 with 5μA measurement current. It is found that the voltage offset depends linearly on the measurement current, Figure 5.11. The origin of this offset is under investigation.

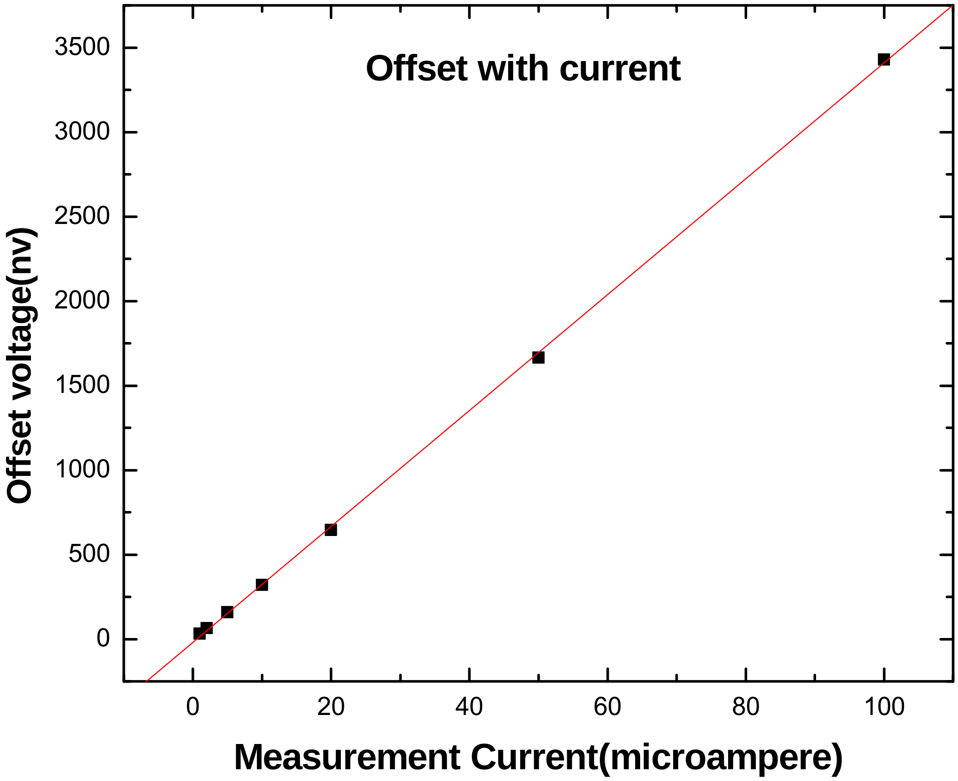

Figure 5.11 Offset linearly depends on measurement current

When using larger measurement current, this offset voltage increases. A larger measurement scale of the Lock-in amplifier has to be used to avoid signal overloading. Measurement resolution decreases if using larger measurement scales. One method to solve this problem, increasing measurement current resulting in lower measurement sensitivity, is to offset the measurement signal against a stable reference signal. The signal to be measured is fed into Channel A of the Lock-in amplifier. The reference signal is fed into Channel B of the Lock-in. The Lock-in amplifier measures the difference between the two signals if using the measurement mode A-B. If the reference signal is very stable, the output of the Lock-in amplifier measures mainly the variation of the signal in Channel A. The reference signal used in this measurement is from a home-built voltage divider. The reference signal was tested, Figure 5.12. The reference signal is very stable after 10 minutes. The stability is about $\frac{0.5\mu v}{3000\mu v} = 0.02\%$. The raw data in Figure 5.12 has 0.5 microvolt variation. This is due to the digitalization limitation of the hp multimeter, and this can be improved by using higher resolution voltmeter to measure the output of the Lock-in amplifier.

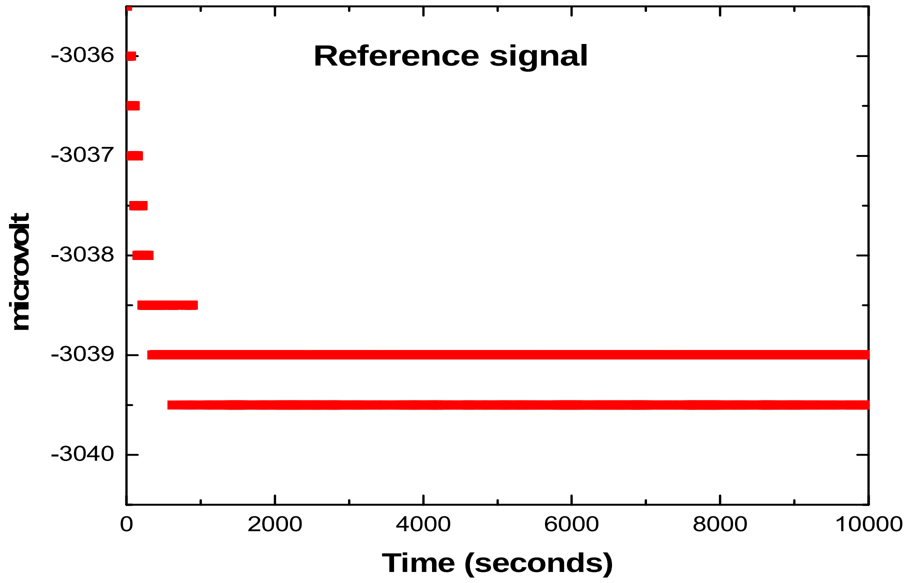

Figure 5.12 Test reference signal. The data is stable after first 10 minutes.

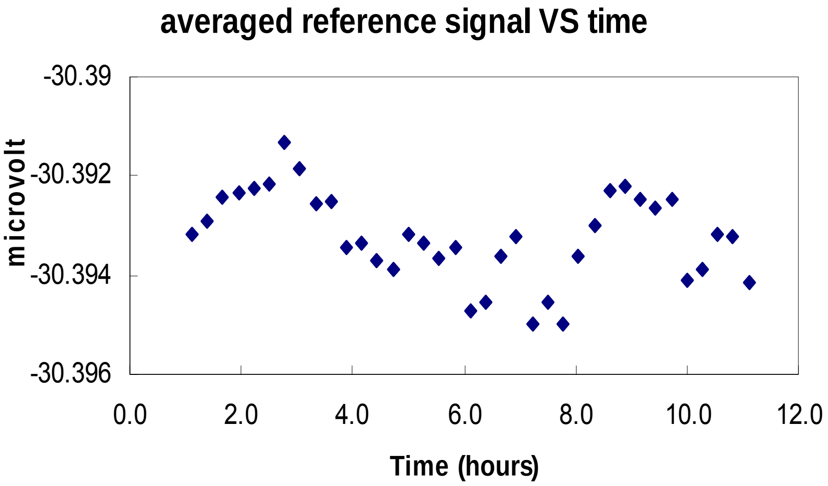

Figure 5.13 Reference signal measured with time.
Each point is the average of raw data for four minutes.

All measurement data is averaged over four minutes to increase resolution, so does the reference signal. The variation of the reference signal averaged over four minutes is small, shown in Figure 5.13. It has a Peak-Peak variation of 4 nanovolt. The variation of the average reference signal in every hour is typically less than 1 nanovolt.

Using reference signal to decrease the absolute value of the voltage, the sample can be measured at higher current. The amplitude of the reference signal is adjusted for every measurement current if needed. The sample S012708 was measured at 5μA using this reference signal, Figure 5.14. The measurement scheme is in Figure 5.10.

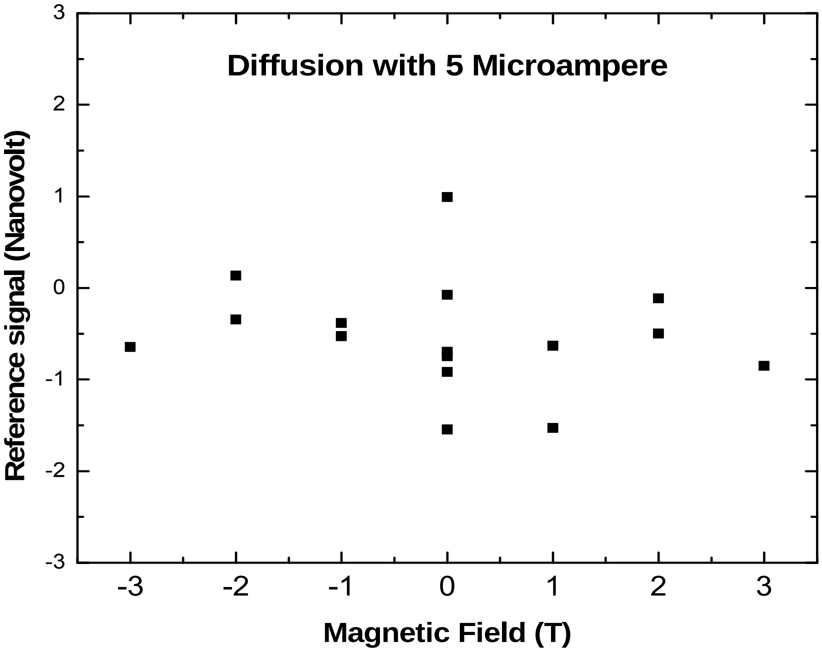

Figure 5.14 Diffusion measurement in magnetic field with 5μA measurement current

At 5μA measurement current, V_{SH} does show a clear dependence with magnetic field, Figure 5.14. The values in zero field were measured at different direction of magnetization of the nickel rod. The variation is about 2.5nv, which is in the order of the measurement sensitivity. The measurement current was increased to 50μA. A tiny quadratic reproducible dependence with magnetic field was observed, Figure 5.15. Similar quadratic dependence was observable with 200μA measurement current. The origin of the quadratic dependence is not clear. It may relate to the offset voltage in Figure 5.11. In the diffusion measurement scheme, no current flew to the right side of the horizontal current strip. The offset may relate to the inhomogeneous diffusive electrons in the copper film near the nickel rod.

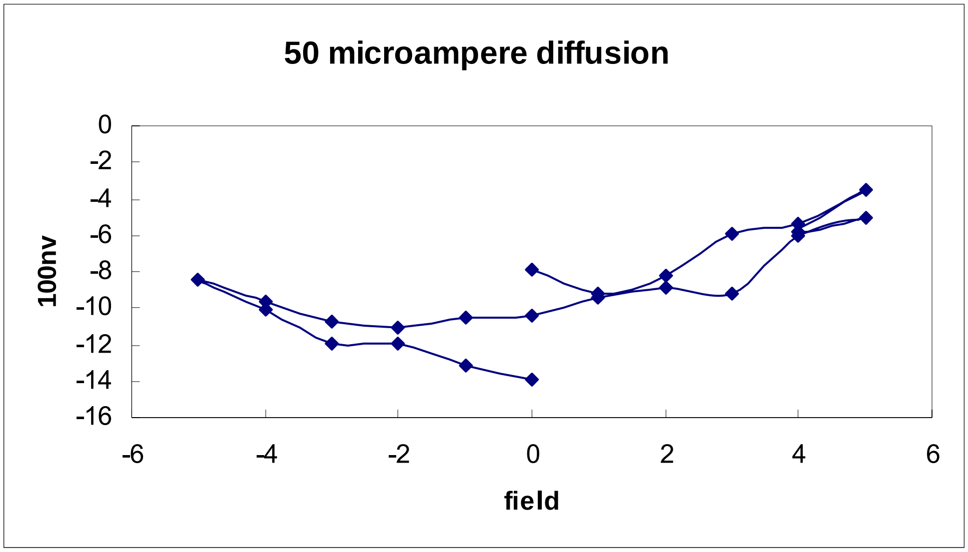

Figure 5.15 Voltage signal in magnetic field at 50μA measurement current

The voltage variation in zero magnetic field in Figure 5.15 is about 4nv only, which is about in our measurement sensitivity. More measurement at zero magnetic field and with different magnetization directions was performed with100μA measurement current. The results are summarized in Table 5, where M↑ (M↓) is the magnetization of the nickel rod if applying a positive (negative) magnetic field and then removing the field.

Table 5 Spin Hall voltage measurement in different nickel magnetizations

Nickel magnetization	M↑	M↓	M↑	M↓	M↑
voltage (nanovolt)	-6.16	-6.5	-6.63	-4.88	-4.01

From Table 5, we do not observe significant difference in difference magnetization directions. The voltage variation in different magnetization direction is smaller than 2nv.

The Spin Hall Effect resistance is derived in [23],

$$\Delta R_{SH} = \frac{\Delta V}{I} = \frac{P\sigma_{SH}}{t{\sigma_c}^2}\exp(-\frac{L}{Lsf}) \tag{5.1}$$

where ΔV is the voltage difference between up and down magnetization directions in Figure 1.8, I is the measurement current, P is the current polarization rate, σ_{SH} is the Spin Hall conductivity. σ_c is the conductivity of the studied film, L is the distance between the injection electrode and the hall cross, L_{sf} is the spin diffusion length of the studied film.

In our system, ΔV is less than 2nv. ΔR_{SH} is less than $\frac{2nv}{100\mu A} = 20\mu\Omega$. In equation (5.1), P and L_{sf} are unknowns. σ_{SH} of copper was $2.4*10^4(\Omega\bullet m)^{-1}$ measured by *T*. Kumura [36], t=25nm, $\sigma_c=6*10^6(\Omega\bullet m)^{-1}$, L is the distance between the nickel rod and the two voltage probes. L was estimated by measuring voltage between pad 1 and 6 with current from pad 2 to 5 in Figure 5.10. The voltage was 55µv with 1µA measurement current. The distance L was estimated as 700nm using the resistivity of copper obtained earlier this section. Eq. (5.1) becomes

$$2\times10^{-5} \geq \frac{P\times2.4\times10^4}{25\times10^{-9}\times(6\times10^6)^2}\exp(-\frac{0.7}{L_{sf}}) \tag{5.2}$$

$$2\times10^{-5} \geq 0.027P\exp(-\frac{0.7}{L_{sf}}) \tag{5.3}$$

From the experiment, the relation (5.3) between P, L_{sf} in our system is obtained. L_{sf} is 1µm[33] for a 50nm thick copper system. The sample in this experiment is 25nm thick. L_{sf} is expected smaller than 1µm. The polarization rate in [23] is 0.28 for a ferromagnetic electrode with a tunnel junction. A permalloy in direct with gold nanostructure [32] has polarization rate of 3%. Our system is similar to [32]. It is possible that the polarization in our system is not bigger than 3%. Possible values of P, L_{sf} are plotted in Figure 5.16.

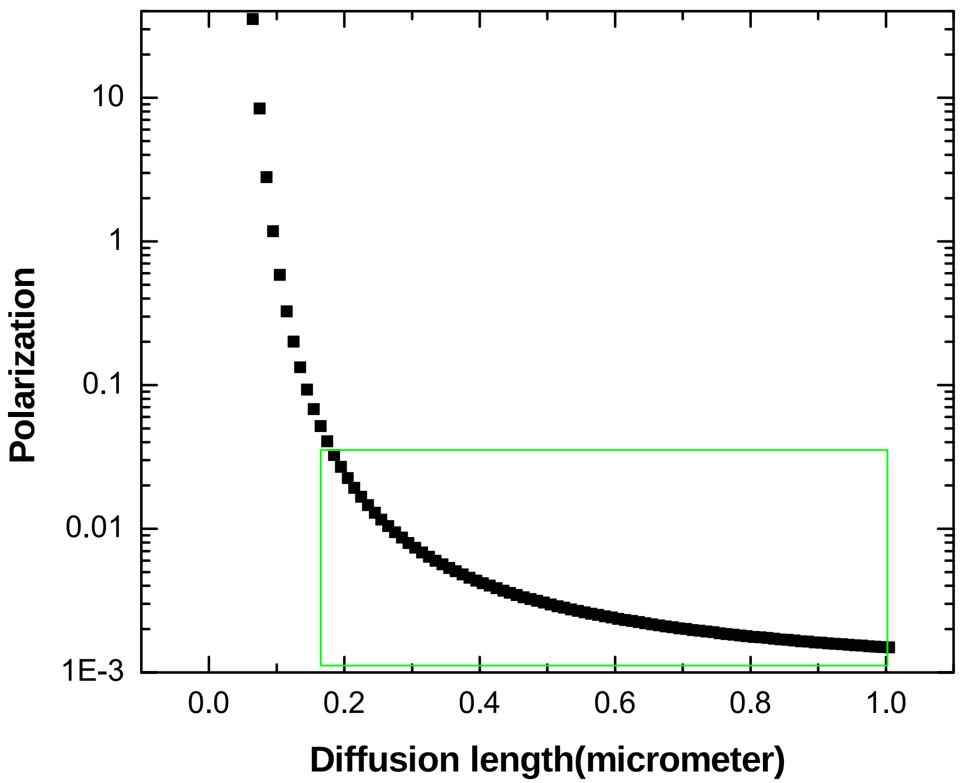

Figure 5.16 Estimation of polarization and spin diffusion length in copper sample

The Spin Hall Effect is not observed in sample S012708. One possibility reason is that the separation distance *L* is bigger than the spin diffusion length L_{sf}, which leads to small signal. The resistance of the electroplated nickel rod is about 89Ω. Lower resistance of the nickel rod has been observed before. The resistance of the nickel rod in Section 5.1.1 is about 10Ω. This may indicate that the nickel rod of sample S012708 is slightly oxidized, which may decrease the polarization. nickel has been used as spin injection in other system. The spin polarization of nickel has been reported as 5~30%[58] in a tunneling experiment. It is worth the effort to continue this work by making samples with short separation distance and lower nickel resistance. The sample fabrication method is too difficult. Further process optimization is preferred. Better experimental methods are always desired.

CHAPTER VI

SUMMARY AND DISCUSSION

The main objective of this work is to detect Spin Hall Effect in paramagnetic thin films. Two generations of experiments were presented. Phase I experiment was presented in chapter III, where Spin Hall Effect in micrometer size aluminum and gold patterns was studied. The samples were fabricated by one step photolithography, deposition and liftoff, which removed interface resistance and alignment challenges. The resistivity of thin film is much larger than the values for a single crystal bar, which leads to much smaller Spin Hall Effect signal. The spin diffusion length of gold thin film is reported as 63 ± 15nm in 2004. The dimension of the gold samples studied in Chapter III is much larger than the spin diffusion length of gold. The phase I experiments were conducted from 2001 to 2004 before any of the experimental works described in Chapter I were published. The Spin Hall Effect in Phase I experiment is a second order effect, and the signal is re-estimated to be smaller than the thermal noise of the system according to experimental values.

In Phase II experiments, tri-layer samples were fabricated using a complicated multi-step process which includes two E-Beam Lithography steps, two or three thin film deposition steps, lift off, and electroplating. The nickel nanorod was positioned perpendicular to the bottom gold or copper thin film pattern. This nickel rod was used as a spin injector. The up limit of the Spin Hall Effect in Sample S012708 was less than 2 nanovolt, possibly due to larger separation distance and high nickel resistance. It may worth the effort to continue this work by making new samples with smaller separation distance and lower the nickel nanorod resistance. Other ferromagnet material with higher polarization rate may be used. The fabrication process may be optimized to achieve higher fabrication yield.

The sample fabrication in Phase II experiments has benefited other experimental groups. The fabrication method has been adopted by Dr. Igor Lyuksyutov and Dr. Naugle's groups to study the magnetic nanodot imaging and to study the interaction between nano dots and superconductors. This fabrication method may also be useful to study perpendicular spin injection, transportation, and detection in other systems.

It has to be pointed out that this sample fabrication involves multi-steps process which complicates the process. The yield is low, especially the electroplating process. In this experiment, optical microscope is used to control the electroplating process. Samples are taken out of the electroplating solution to determine the plating level. For materials especially at nanometer scale, this step may involve significant oxidation due to larger surface to volume ratio. A better optical microscope which can monitor the electroplating process in situ is ideal for this fabrication process.

It is very difficult to fabricate 3d dimensional structures using electron beam lithography and electroplating. Sophisticated systems that can better control perpendicular nanostructure growth are useful. A low temperature STM system with spin polarized tunneling is a powerful tool to study Spin Hall Effect. With a ferromagnetic STM tip magnetized in situ, perpendicular spin polarized current is easily injected into a paramagnetic system. The distance between the STM tip and a hall cross can be changed easily and this distance can be varied in one sample. There is no need to make huge amount of samples with changing distance. Spin polarized tunneling has a higher polarization rate in a similar system [58]. The Spin Hall Effect signal may be much larger.

The signal in this experiment is small. It is better to amplify the signal at lower temperature. It is a good idea to integrate an amplifier circuit on the chip. This method requires strong circuit design and process development skills.

Fundamental research in Spintronics will continue to be a hot subject in the near future. The Spin Hall Effect has been demonstrated in recent years. It is time to aim at applications which requires extensive collaborations within various disciplines and the industry.

REFERENCES

1. S. F. Zhang, W. G. Kuch, G. Guntherodt, C. Broholm, A. D. Kent, M. R. Fitzsimmons, I. K. Schuller, J. B. Kortright, T. Shinjo and Y. M. Zhu, eds. *Magnetoelectronics and Magnetic Materials--Novel Phenomena and Advanced Characterization* (Materials Research Society: Warrendale, Pennsylvania, 2002).

2. S. A. Wolf, D. D. Awschalom, R. A. Buhrman, J. M. Daughton, S. V. Molnar, M. L. Roukes, A. Y. Chtchelkanova and D. M. Treger, Science, **294**, 7 (2001).

3. S. A. Wolf and D. Treger, IEEE Transactions on Magnetics, **36**, 2748 (2000).

4. D. D. Awschalom, D. Loss and N. Samarth eds. *Semiconductor Spintronics and Quantum Computation* (Springer, Berlin, New York, 2002).

5. M.E. Flatte, IEEE Transactions on Electron Devices, **54**, 907 (2007).

6. S. A. Wolf, A.Y. Chtchelkanova and D.M. Treger, IBM Journal of Research & Development, **50**, 101 (2006).

7. B. A. Bernevig and S. Zhang, IBM Journal of Research & Development, **50**, 141 (2006).

8. M. N. Baibich, J. M. Broto, A. Fert, F. Nguyen Van Dau, F. Petroff, P. Eitenne, G. Creuzet, A. Friederich and J. Chazelas, Physical Review. Letters, **61**, 2472 (1988).

9. G. Binasch, P. G.runberg, F. Saurenbach and W. Zinn, Physical Review B, **39**, 4828 (1989).

10. H. Ehrenreich and D. Turnbull, eds. *Solid State Physics* (Academic Press, Cambridge, Massachusetts , 1994), **47**, p. 367-462.

11. S. Datta and B. Das, Applied Physics Letters, **56**, 665 (1990).

12. M. I. Dyakonov and V. I. Perel, Physics Letters A, **35**, 459 (1971).

13. M. I. Dyakonov and V. I. Perel, JETP Letters, **13**, 3 (1971).

14. J. E. Hirsch, Physical Review Letters, **83**, 1834 (1999).

15. S. F. Zhang, Physical Review Letters, **85**, 393(2000).

16. M. Shuichi, N. Nagaosa and S. C. Zhang, Science, **310**, 1348 (2003).

17. J. Sinova, D. Culcer, Q. Niu, N.A. Sinitsyn, T. Jungwirth and A. H. MacDonald, Physical Review Letters, **92**, 126603 (2004).

18. J. Sinova, S. Murakami, S. Q. Shen and M. S. Choi, Solid State Communications, **138**, 214 (2006).

19. C. M. Hurd, *The Hall Effect in Metals and Alloys*, (Plenum Press, New York, 1972).

20. K. Robert and J. M. Luttinger, Physical Review, **95**, 1154 (1954).

21. Y. K. Kato, R. C. Myers, A. C. Gossard and D. D. Awschalom, Science, **306,** 1910 (2004).

22. J. Wunderlich, B. Kaestner, J. Sinova and T. Jungwirth, Physical Review Letters **94**, 047204 (2005).

23. S. O. Valenzuela and M. Tinkham, Nature, **442**, 176 (2006).

24. T. Kimura, Y. Otani, T. Sato, S. Takahashi and S. Maekawa, Physical Review Letters, **98**, 156601 (2007).

25. V. Sih, R. C. Myers, Y. K. Kato, W. H. Lau, A. C. Gossard and D. D. Awschalom, Nature Physics, **1**, 31 (2005).

26. N. P. Stern, S. Ghosh, G. Xiang, M. Zhu, N. Samarth and D. D. Awschalom, Physical Review Letters, **97**, 126603 (2006).

27. T. N. Morgan, Physical Review, **148**, 890 (1966).

28. S. O. Valenzuela and M. Tinkham, Applied Physics Letters, **85**, 5914 (2004).

29. S. O. Valenzuela, D. J. Monsma, C. M. Marcus, V. Narayanamurti and M. Tinkham, Physical Review Letters, **94**, 196601 (2005).

30. F. J. Jedema, H. B. Heersche, A. T. Filip, J. J. A. Baselmans and B. J. van Wees, Nature, **416**, 713 (2002).

31. M. Johnson and R. H. Silsbee, Physical Review Letters, **55**, 1790 (1985).

32. Y. Ji, A. Hoffmann, J. S. Jiang and S. D. Bader, Applied Physics Letters, **85**, 6218 (2004).

33. F. J. Jedema, A. T. Filip and B. J. van Wees, Nature, **410**, 345 (2001).

34. M. Johnson and R. H. Silsbee, Physical Review B, **37**, 5312 (1988).

35. M. Johnson and R. H. Silsbee, Physical Review B, **37**, 5326 (1988).

36. T. Kimura, J. Hamrle and Y. Otani, Physical Review B, **72**, 014461 (2005).

37. T. Kimura, Y. Otani and J. Hamrle, Physical Review B, **73**, 132405 (2006).

38. P. V. Zant, *Microchip Fabrication: A Practical Guide to Semiconductor Processing*, 4th Ed. (McGraw-Hill, New York, 2000).

39. H. H. Wieder, *Laboratory Notes on Electrical and Galvanomagnetic Measurements* (Elsevier, New York, 1979).

40. J. Yeager and M. A. Hrusch-Tupta eds *Low Level Measurement Handbook,* 6th Ed., (Keithley, Cleveland, Ohio, 2004)

41. M. J. Madou, *Fundamentals of Microfabrication*. 2nd Ed. (CRC Press, Boca Raton, Florida, 2002).

42. C. Arnone, Microelectronic Engineering, **17**, 483 (1992).

43. G. Sauerbrey and Z. Fur, Physik, **155**, 206 (1959).

44. H. Qiu, F. P. Wang, P. Wu, L. Q. Pan, L. Y, Li, L. Y. Xiong and Y. Tian, Thin Solid Films, **414**, 150 (2002).

45. C. Kittel, *Introduction to Solid State Physics*, 7th Ed. (Wiley, New York, 1996).

46. G. Kästle, H. G. Boyen, A. Schröder, A. Plettl and P. Ziemann, Physical Review B, **70**, 165414 (2004).

47. A. G. Aronov, JETP Letters, **24**, 32 (1976).

48. R. H Silsbee and M. Johnson, Physical Review B, **37,** 5312 (1988).

49. M. Johnson and J.Byers, Physical Review B, **67**, 125112 (2003).

50. S. O. Valenzuela and M. Tinkham, Journal of Applied Physics, **101**, 09B103 (2007).

51. W. Xu, J. Wong, C. C. Cheng, R. Johnson and A. Scherer, Journal of Vacuum Science and Technology B, **13**, 2372 (1995).

52. S. Y. Chou, P. R. Krauss and L. Kong, Journal of Applied Physics, **79**, 6101 (1996).

53. R. O'Barr, S. Y. Yamamoto, S. Schultz, W. H. Xu and A. Scherer, Journal of Applied Physics, **81**, 4730 (1997).

54. W. H. Wu, J. B. Dimaria, H. G. Yoo, S. L. Pan, L. J. Rothberg and Y. Zhang, Applied Physics Letters, **84**, 966 (2004).

55. L. Piraux, S. Dubois, E. Ferain, R. Legras, K. Ounadjela, J. M. George, J. L. Maurice and A. Fert, Journal of Magnetism and Magnetic Materials, **165**, 352 (1997).

56. P. R. Krauss, P. B. Fischer and S. Y. Chou, Journal of Vacuum Science and Technology B, **12**, 3639 (1994).

57. M. N. Ou, T. J.Yang, S. R. Harutyunyan, Y. Y. Chen, C. D. Chen and S. J. Lai, Applied Physics Letters, **92**, 063101 (2008).

58. S. F. Alvarado and P. Renaud, Physical Review Letters, **68**, 1387 (1992).

VITA

Huachun Xu was born in P. R. China in October 1979. He received his B.S. degree in physics from the University of Science and Technology of China in July 2001. In September 2001, he enrolled in the Physics Department at Texas A&M University. He conducted his Ph.D. research under the direction of Winfried Teizer and received his Ph.D. degree in December 2008, from Texas A&M University.

Department of Physics
c/o Dr. Winfried Teizer
Texas A&M University
College Station, TX 77843-4242